Fluid pumping of peristaltic vessel fitted with elastic valves

Ki Tae Wolf 1, J. Brandon Dixon 1,2,3, Alexander Alexeev 1,*

George W. Woodruff School of Mechanical Engineering,
Petit Institute for Bioengineering and Bioscience,
Wallace H. Coulter Department of Biomedical Engineering,
Georgia Institute of Technology, Atlanta, GA 30332

Abstract

Using numerical simulations, we probe the fluid flow in an axisymmetric peristaltic vessel fitted with elastic bi-leaflet valves. In this biomimetic system that mimics the flow generated in lymphatic vessels, we investigate the effects of the valve and vessel properties on pumping performance of the valved peristaltic vessel. The results indicate that valves significantly increase pumping by reducing backflow. The presence of valves, however, increases the viscous resistance therefore requiring greater work compared to valveless vessels. The benefit of the valves is the most significant when the fluid is pumped against an adverse pressure gradient and for low vessel contraction wave speeds. We identify the optimum vessel and valve parameters leading to the maximum pumping efficiency. We show that the optimum valve elasticity maximizes the pumping flow rate by allowing the valve to block more effectively the backflow while maintaining low resistance during the forward flow. We also examine the pumping in vessels where the vessel contraction amplitude is a function of the adverse pressure gradient as found in lymphatic vessels. We find that in this case the flow is limited by the work generated by the contracting vessel, suggesting that the pumping in lymphatic vessels is constrained by the performance of lymphatic muscle. Given the regional heterogeneity of valve morphology observed throughout the lymphatic vasculature, these results provide insight into how these variations might facilitate efficient lymphatic transport in the vessel's local physiologic context.

1. Introduction

The lymphatic system is responsible for transportation of interstitial fluid, lipids, and immune cells to maintain homeostasis throughout the body. Interstitial fluid and macromolecules collected

^{*} Email: alexander.alexeev@me.gatech.edu; Phone: 404-385-3659; Fax: 404-894-8496

and circulated by the lymphatic system join the blood circulatory system to maintain tissue fluid balance and waste management. Fatty acid is collected in the gut from food, packaged into chylomicrons, and transported via the lymphatic system as the primary route of lipid trafficking to the peripheral tissues, and transported immune cells and antigens provide a proper immune response (Dixon, 2010; Swartz, 2001). Nearly all tissues in the body critically rely on the lymphatic system for proper operation, yet this is achieved without a centralized pump and under an adverse pressure gradient. Instead, circulation is achieved by a combination of nearby tissues' skeletal muscular movement (extrinsic pump) (Ikomi & Schmid-Schonbein, 1996; McGeown et al., 1988; Reddy et al., 1981; Skalak et al., 1984; Webb Jr & Starzl, 1953) and a series of contracting vessels and valves throughout the collecting lymphatics known as the intrinsic lymphatic pump (Davis et al., 2011; Quick et al., 2007; Zawieja, 2009). The intrinsic lymphatic pump is composed of chains of contractile units called lymphangions, defined as a region of lymphatic vessel separated by two lymphatic valves. For an efficient transport of lymphatic fluids in the desired direction, lymphatic valves play a critical role by reducing backflow and maximizing the net flow, often against a gravitational load.

Dysfunction of lymphatic valves or smooth muscles that drive contractile motion of the lymphatic vessels can lead to debilitating conditions of lymphedema, for which there is currently no cure (Mortimer & Rockson, 2014). Palliative treatment options such as compression garments do exist, but these methods only seek to relieve the symptoms of disease without addressing the underlying cause. In some cases like genetic primary lymphedema, lymphatic valve defects have been identified as a major source of dysfunction (Brouillard et al., 2014; Davis et al., 2012; Eisenhoffer et al., 1995; Lapinski et al., 2017; Petrova et al., 2004; Sabine et al., 2015). While many of these studies have identified the molecular mechanism responsible for the morphologic valve defect, the structure-function relationship of lymphatic valves and the exact consequence of subtle valve defects on the pump performance of the lymphatic network are less understood. In addition, the role that factors like the heterogeneity of lymphatic valves play has been studied but is still largely unknown.

To address this limited understanding, computational studies have been providing valuable insights in creating a detailed picture of lymphatic operation and has indicated that lymphatic valve's properties affect the pumping performance of the lymphatic system (Bertram et al., 2014b; Davis et al., 2011; Wilson et al., 2015). These computational studies range from lumped-parameter

models that solve differential equations combined with experimental data (Baish et al., 2016; Bertram et al., 2011; Bertram et al., 2014a; Bertram et al., 2014b; Bertram et al., 2016; Jamalian et al., 2013; Jamalian et al., 2016; Razavi et al., 2017; Reddy et al., 1977) to multi-dimensional studies of fluid and solid components involved in lymph flow (Bertram, 2020; Kunert et al., 2015; MacDonald et al., 2008; Rahbar & Moore, 2011; Wilson et al., 2015). However, many of these studies employ assumptions or simplifications particularly in regard to valve behavior, providing only a limited understanding of the role of lymphatic valve to lymphatic transport performance and efficiency. For example, the lumped-parameter model or zeroth-dimensional study utilizes a valve resistance curve that is an empirical fit of lymphatic valve behavior based on a single experimental data (Bertram et al., 2011). Most of these studies can effectively simulate chains of lymphangions, thus revealing large-scale behaviors of lymphangion networks. But because of the rarity of measured lymphatic valve properties (Lauweryns & Boussauw, 1973; MacDonald et al., 2008; Pan et al., 2011; Wilson et al., 2015), the empirical fit that describes the lymphatic valve's flow response is limited in describing lymphatic performance and efficiency under different valve properties such as valve length and stiffness.

Higher dimensional models of the lymphatic system can address this limitation by modeling the lymphatic valve based on more readily available geometric profile of the valve (Bertram, 2020; Wilson et al., 2015), but these models also simplify the physics through assumptions such as a steady flow condition (Wilson et al., 2015), exclusion of components that require fluid-structure interaction like the lymphatic valves (Rahbar & Moore, 2011), or using externally applied fluid flow (Bertram, 2020). We recently conducted three-dimensional simulations using a fully-coupled fluid-structure interaction model to probe the behavior of compliant lymphatic valves in a fluid flow (Ballard et al., 2018). Valves with different geometries and mechanics were placed in a rigid axisymmetric vessel and flow was induced by applying oscillating or unidirectional pressure gradients. It was found that shorter valves have a lower flow resistance, however when the valves are too short, they are unable to fully occlude the backflow, indicating the existence of an optimal valve length. It was also shown that more flexible valves cause a lower resistance to the flow. Furthermore, under oscillating flow, valve elasticity leads to a delay in valve response that has been reported in experiments (Davis et al., 2011).

In this paper, we focus on understanding the pumping behavior of a peristaltically contracting vessel fitted with compliant valves similar to those found in lymphatic systems (Ohhashi et al.,

1980; Zawieja et al., 1993). We consider a periodic vessel that undergoes periodic radial contractions leading to a sinusoidal traveling wave (Shapiro et al., 1969; Takabatake et al., 1988). We use this model to investigate the effects of elastic valves on pumping performance of peristaltically contracting vessels. Specifically, valve and vessel properties such as vessel contraction wave speed, vessel contraction amplitude, and valve elasticity are systematically probed for the peristaltic pumping under a range of applied adverse pressure gradients.

Additional complexity in lymphatic systems emerges due the coupling between the contraction amplitude of lymphatic vessel and the applied adverse pressure gradient (Davis et al., 2012). Experiments show that an increasing adverse pressure gradient results in a decreased contraction amplitude diminishing the pumping performance of lymphatic vessel. Such behavior is typically associated with the finite force generation by the lymphatic muscle cells driving contractions. Other physiological features affecting lymphatic pumping include nonuniformity of vessel contraction near the valve (Akl et al., 2011; Davis et al., 2012) and lymph flow-sensitive wall contraction via wall shear stress (Gashev et al., 2002; Kornuta et al., 2015). Here, we examine how the coupling between the adverse pressure gradient and the vessel contraction amplitude affects the pumping performance of peristaltic vessels with elastic valves.

Without valves, peristaltic pumping generates fluid packets with alternating axial velocity that are steady in the moving frame of reference under constant contraction wave speed c (Figure 1a). These velocity packets lead to a net transport of the fluid in the direction of wave propagation that we refer as the positive flow direction. The presence of an adverse pressure gradient can reduce the net fluid pumping by peristaltic oscillations and ultimately can result in a negative flow (Figure 1b). When the adverse pressure gradient is large enough, sections with positive flow velocity diminish or entirely disappear, even though the general pattern with repeating velocity packets is still maintained (Figure 1c). The peristaltic pumping in a vessel without valves provides a baseline that allows us to evaluate the function of valves and to identify their effects on the fluid flow and pumping.

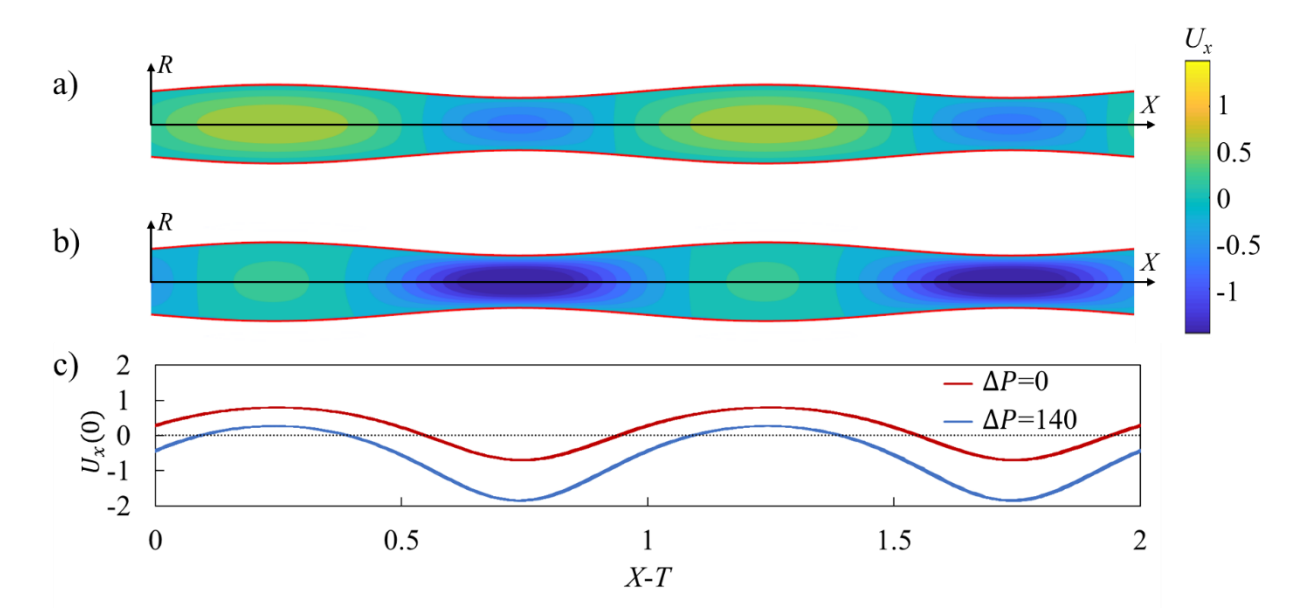


Figure 1. a) Axial component of flow velocity U_x in a valve-less peristaltic vessel without an imposed pressure gradient yielding a flow rate Q=0.15. b) Axial velocity U_x in a vessel with an adverse pressure gradient $\Delta P=140$ yielding a flow rate Q=-0.22. c) Centerline axial velocity $U_x(0)$ in the moving reference frame X-T. In these simulations, the contraction ratio is $\phi=0.2$, and the peristaltic Reynolds number is Re=0.2. Note that $X=x/\lambda$, $T=t/\tau$, $\Delta P=\Delta p_\lambda r_0^2 \rho/\mu^2$ $Q=q/\pi r_0^2 c$, $\phi=\frac{a}{r_0}$, and $Re=\rho c r_0^2/\mu\lambda$, where Δp_λ is the pressure difference across a contraction wavelength, q is the vessel flow rate, r_0 is the mean radius of the vessel, x is the axial coordinate, x0 and x1 are the fluid density and dynamic viscosity, and x2 is time. Furthermore, x2, x3, x4, x5, x6, and x7 are the wavelength, period, speed, and amplitude of vessel contraction. See Video S1 in SI.

The paper is organized as follows. In Section 2, we present our computational methodology and the model validation. This section also describes the relevant model parameters. The simulation results are reported and discussed in Section 3. Section 3.1 compares peristaltic pumping in vessels with and without valves to identify the effects of valve on the flow pattern and pumping performance. Section 3.2 investigates the effect of vessel contraction speed on flow behavior and pumping performance. Section 3.3 studies the effect of an adverse pressure gradient, while Section 3.4 examines the effect of valve elasticity on the pumping performance. Section 3.5 considers the effects of coupling between the adverse pressure gradient and the amplitude of vessel contractions on the fluid pumping. Our conclusions are summarized in Section 4.

2. Methodology

To model viscous fluid flow within a peristaltic vessel fitted with elastic valves, a fully coupled three-dimensional fluid-structure interaction solver (FSI) is used. A lattice Boltzmann model (LBM) and a lattice spring model (LSM) are used to simulate the fluid mechanics and solid mechanics, respectively. To capture interactions between fluid and solid, the models are coupled through the boundary conditions as implemented previously (Alexeev et al., 2005; Alexeev & Balazs, 2007).

LBM efficiently simulates incompressible viscous flows (Ladd & Verberg, 2001; Succi, 2001) and is well suited for studies with complex, moving geometries, such as compliant valves and contracting vessels. LBM simulates the Navier-Stokes equations at mesoscale by integrating the time evolution of the velocity distribution function representing fluid "particles" moving on a fixed lattice $f_i(\mathbf{r},t)$, where i, \mathbf{r} , and t are the velocity direction, the lattice position, and time, respectively. The distribution function is integrated over discrete time steps via streaming and collision of "particles", where fluid "particles" travel across the lattice in a given speed and direction. In this work, we use BGK collision operator and a D3Q19 grid representing a three-dimensional system with 19 discrete velocity directions. Hydrodynamic fields such as density, momentum, and stresses are evaluated by taking moments of the distribution function.

Solid components of the system are modelled using LSM (Buxton et al., 2005; Ostoja-Starzewski, 2002). We represent thin elastic valve material as an infinitely thin elastic plate discretized using a network of masses linked by stretching and bending springs. Solid nodes are arranged in a regular triangular lattice with nearby nodes connected via a linear stretching spring of in-plane stiffness k_s . The bending of the plate is modeled through a series of bending springs with bending stiffness k_b , which connect three neighboring LSM nodes. The related macroscopic properties, such as Young's modulus and bending rigidity, are defined using the in-plane and bending stiffnesses as $e_s = 2k_s/\sqrt{3}$ (Ostoja-Starzewski, 2002) and $d_b = 3\sqrt{3}k_b/4$, respectively (Buxton et al., 2005).

LBM and LSM interact through a two-way coupling at fluid-solid boundaries with the momentum exchange approach. The momentum due to fluid-solid interaction is transferred to fluid using interpolated bounce-back rule and distributed through corresponding solid nodes via applied forces to ensure momentum conservation (Alexeev et al., 2005; Alexeev et al., 2006; Mao &

Alexeev, 2014). This method of coupling has been previously extensively validated with different FSI problems (Ballard et al., 2018; Hanasoge et al., 2017; Mao & Alexeev, 2014; Masoud et al., 2012; Yeh & Alexeev, 2016).

Initial geometry of the model is composed of a periodic fluid-filled axisymmetric vessel and two sets of valves with each valve made up of two compliant leaflets (Figure 2). Each leaflet is created from an intersecting plane between an axisymmetric vessel and a plane that cuts through the vessel at an angle (Ballard et al., 2018). Thus, the elastic leaflets are initially flat. The leaflet edge that overlaps with the vessel wall is firmly attached to the wall and follows the wall motion. The free edge of the leaflet has a semicircular cutout mimicking the typical geometry observed for lymphatic valves (Watson et al., 2017). The valve geometry combined with the axisymmetric vessel deem it necessary to use of a three-dimensional computational model since lower dimensional or axisymmetric models are unable to capture the leaflet motion. The leaflet geometry is characterized by the aspect ratio that is defined as the ratio between axial length of the leaflet and mean diameter of the vessel. In this work, we keep the leaflet aspect ratio equal to 1.75 that is in the typical range of experimental values (Ballard et al., 2018). The simulation domain has 301 by 44 by 44 LBM nodes in x, y, and z-directions, respectively, while the vessel and valves are composed of 8272 LSM nodes. The initial distance between two neighboring LSM nodes is about twice the distance between neighboring LBM nodes.

The vessel undergoes a prescribed radial motion that leads to a sinusoidal traveling wave propagating along the vessel in the axial x direction. The periodic motion of the vessel wall is given by $r_{vess}(x,t) = r_0 \left[1 + \phi \sin \left(\frac{2\pi}{\lambda} (x - ct) \right) \right]$, where r_0 is the mean radius of the vessel, ϕ is the normalized contraction amplitude, λ is the wavelength, and $c = \lambda/\tau$ is the wave speed with τ being the oscillation period. Note that $\phi = \frac{a}{r_0}$ where a is the vessel contraction amplitude. We set the wavelength equal to the distance between centroids of two consecutive valves. The wavelength is kept at a constant value equal to the distance between valves to induce synchronous valve deformation, providing a clearer understanding behind fundamental operation of valves in contracting vessel. We plan to further explore the effect of contraction wave wavelength in our future works.

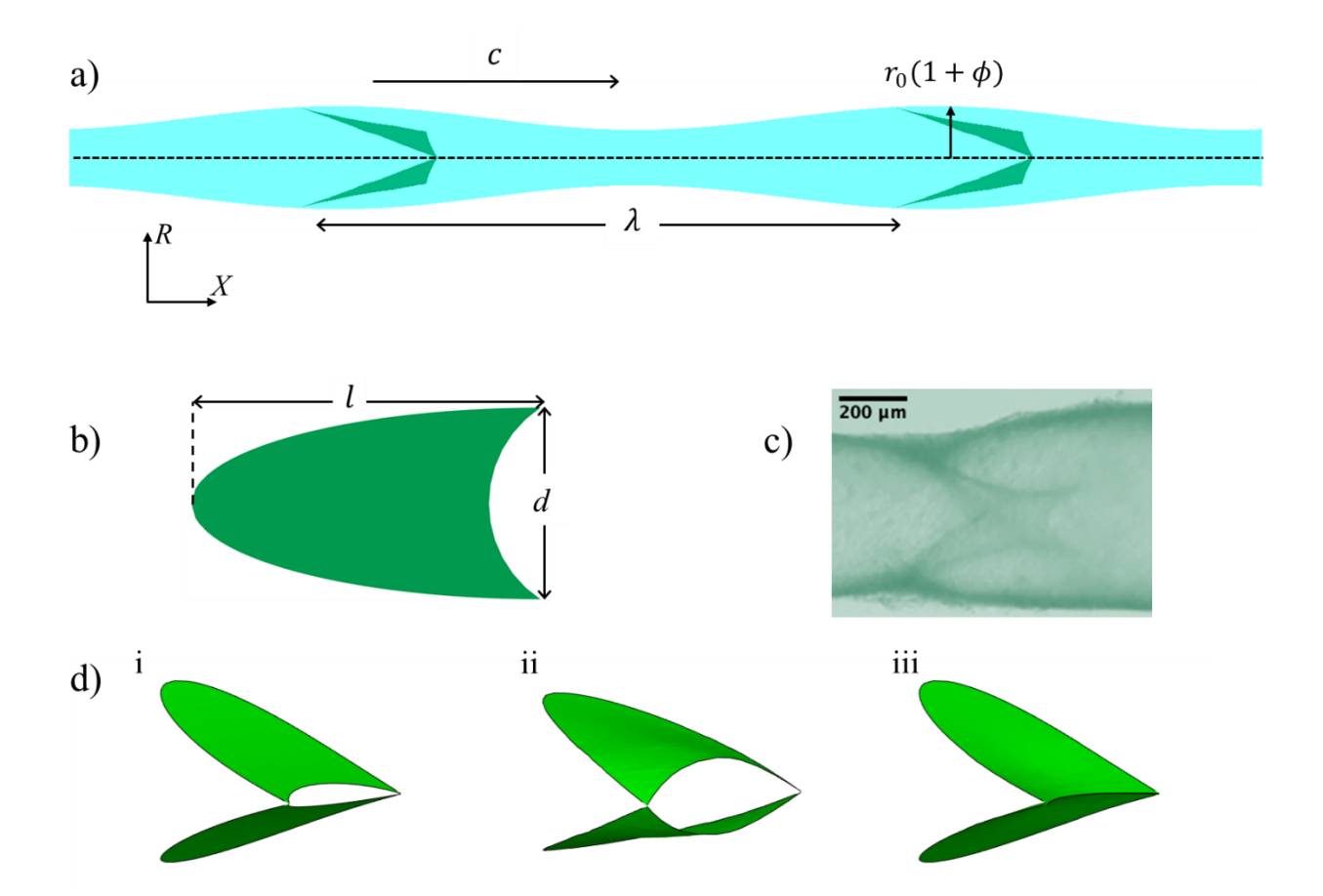


Figure 2. a) Model of a periodic contracting vessel fitted with two valves. b) Shape and dimensions of the valve leaflet. The edge on the right side of the leaflet is free, whereas the remaining part of the edge is attached to the vessel wall. The aspect ratio of the valve is defined as l/d = 1.75. c) Image of a lymphatic vessel segment with a valve. d) Typical valve profiles during different stages of valve operation. i: initial valve configuration, ii: valve opening, and iii: valve closure. See Video S2 in SI.

Experiments report a wide range of the contraction wavelength λ . Indeed, the weave speed c ranges from zero to 10mm/s with the frequency between 7 and 21 contractions per minute yielding the wavelength between 0 and 81mm (Akl et al., 2011; MacDonald et al., 2008). Since the vessel diameters typically range from $80\mu m$ to 2.8mm and considering that the larger vessels exhibit a longer wavelength, we estimate that the ratio of the wavelength to the vessel radius λ/r_0 is in a wide range between 0 and 60. In our simulations, we set $\lambda/r_0 = 15$, which falls well in the experimental range. Furthermore, considering that inter-valve distance is the same as λ , this puts the valve placement within the experimental range where the values of this ratio are up to 20 (Margaris & Black, 2012; Pan et al., 2010; Pan et al., 2011). To model lymphatic chain, we use a

periodic boundary condition in the axial direction, simulating an infinitely long repeating chain of valves.

We vary the following system parameters to investigate the vessel pumping performance: the traveling speed of vessel contraction wave c that is varied by varying the contraction period τ , the normalized contraction ratio ϕ , the adverse pressure difference over a contraction wavelength Δp_{λ} , and the in-plane stiffness and the bending stiffness of the valve. The ranges of these system parameters are selected based on the available experimental data summarized in Table 1.

Note that in lymphatic systems, the contraction amplitude depends on the adverse pressure difference Δp_{λ} (Davis et al., 2012). Here, we first examine the flow where the two parameters are independent to isolate the effect of each parameter on the flow. Then, the two parameters are coupled via the experimentally reported relationship and investigated to reveal any difference arising from the coupling.

Table 1 Lymphatic system parameters

Parameters	Experiments	Reference
Valve length, $l (\mu m)$	80~2800 (est.)	Akl et al. (2011); Pan et al. (2011); Rahbar and Moore (2011); Wilson et al. (2015)
Average vessel diameter, d (μm)	80~2800	Akl et al. (2011); MacDonald et al. (2008); Pan et al. (2011); Rahbar and Moore (2011); Wilson et al. (2015)
Valve thickness (μm)	0.5~6	Lauweryns and Boussauw (1973)
Applied adverse pressure difference, Δp_{λ} (Pa)	0~2000	Davis et al. (2011); Davis et al. (2012); Scallan et al. (2012)
Contraction wave speed, c (mm/s)	0~10	Akl et al. (2011)
Contraction frequency, $1/\tau$ (contraction/min)	7~21	Akl et al. (2011)
Dimensionless contraction amplitude, (ϕ)	0~0.45	Davis et al. (2012)
Viscosity, μ ($mPa \cdot s$)	0.89~1.36	Kassis et al. (2016); MacDonald et al. (2008); Moore and Bertram (2018)
Fluid density, ρ (kg/m^3)	998~1016	Burton-Opitz and Nemser (1917); MacDonald et al. (2008); Moore and Bertram (2018)

The above mentioned physical parameters can be expressed in terms of the following dimensionless parameters relevant to peristaltic pumping (Shapiro et al., 1969; Takabatake et al., 1988), which are indicated using the uppercase. We use the dimensionless axial coordinate $X = x/\lambda$, radial coordinate $R = r/r_0$, axial component of flow velocity $U_x = u_x/c$, and time $T = t/\tau$. The adverse pressure difference is nondimensionalized as $\Delta P = \Delta p_\lambda \, r_0^2 \rho/\mu^2$, which represents the ratio between pressure and viscous forces during peristaltic pumping (Böhme & Müller, 2013; Hariharan et al., 2008; Rachid & Ouazzani, 2015; Rao & Usha, 1995; Shapiro et al., 1969; Tripathi, 2013). The Reynolds number for peristaltic pumping is defined as $Re = \rho c r_0^2/\mu\lambda$, where ρ is the fluid density, and μ is the dynamic viscosity (Connington et al., 2009; Pozrikidis, 1987; Shapiro et al., 1969; Takabatake et al., 1988; Zien & Ostrach, 1970). Because parameters that describe Re are kept constant throughout the work except for c, a change in peristaltic Reynolds number means a corresponding change in contraction wave speed defined by τ . We vary Re in the range between 0.1 and 1.4. The dimensionless valve leaflet in-plane and bending stiffnesses are $K_s = \frac{k_s \rho r_0}{\mu^2 r_0}$ and $K_b = \frac{k_b \rho}{\mu^2 r_0}$, respectively. These parameters represent the ratios between, respectively, stretching and bending forces experienced by the valve and the viscous forces applied on the vessel wall.

The pumping performance is quantified in terms of the flow rate q averaged over a wave period τ , the average work done by the vessel wall w_{avg} , pumping efficiency η and pumping economy ε that are both evaluated over a wavelength λ and averaged over a wave period τ . To calculate w_{avg} the work done by vessel walls is calculated by integrating the hydrodynamic force on the wall over the wall displacement and averaging the work over the wavelength λ and period τ of the vessel. The pumping efficiency is defined as $\eta = q\Delta p_{\lambda}\tau/w_{avg}$ while the pumping economy is defined as $\varepsilon = q(\Delta p_{\lambda} + \Delta p_{visc})\tau/w_{avg}$, where Δp_{visc} is pressure loss due to viscous friction for laminar flow arising at flow rate q in a straight pipe with radius r_0 and length λ . This is expressed as $\Delta p_{visc} = q/(\pi r_0^4/8\mu\lambda)$. Thus, the pumping efficiency represents the relative amount of work done by the vessel that goes into the transporting the fluid against the adverse pressure gradient, whereas the flow economy indicates the proportion of the work that is consumed by the fluid transport and viscous losses. The flow rate is normalized as $Q = q/q_0$, where $q_0 = \pi r_0^2 c$ is the flow rate in a rigid pipe with radius r_0 and average flow velocity c. Note that this normalization that has been previously used for peristaltic pumping (Shapiro et al., 1969; Takabatake et al., 1988). Work done by the vessel wall per wave period is normalized by the corresponding friction loss generated in a

rigid pipe with an average flow velocity c using Hagen-Poiseuille law (Sutera & Skalak, 1993) and is given by $W = w_{avg}/(8\mu\lambda\pi c^2\tau)$. To characterize valve opening, we evaluate the cross-sectional area defined by the free edges of the leaflets a_{valve} that is normalized as $A = a_{valve}/\pi r_0^2$. The maximum valve opening A_{max} is defined as the maximum value of A over a vessel cycle. Furthermore, we examine the time that the valve is closed per vessel cycle $T_c = \tau_c/\tau$. Here, τ_c is the time that valve remains closed during one vessel period. The valve is considered closed when A < 0.05. The dimensionless parameters are summarized in Table 2.

Table 2 Definitions of the dimensionless parameters

Dimensionless parameter	Expression		
Input parameters			
Peristaltic Reynolds number	$Re = \rho c r_0^2 / \mu \lambda$		
Contraction amplitude	$\phi = a/r_0$		
Pressure difference	$\Delta P = \Delta p_{\lambda} r_0^{\ 2} \rho / \mu^2$		
Bending stiffness	$K_b = k_b \rho / \mu^2 r_0$		
In-plane stiffness	$K_{\rm S} = k_{\rm S} \rho r_0 / \mu^2$		
Output parameters			
Flow rate	$Q = q/q_0 = q/(\pi r_0^2 c)$		
Work done by the vessel	$W = w_{avg}/(8\mu\lambda\pi c^2\tau)$		
Pumping efficiency	$\eta = q \Delta p_{\lambda} \tau / w_{avg}$		
Pumping economy	$\varepsilon = q(\Delta p_{\lambda} + \Delta p_{visc})\tau/w_{avg}$		
Valve opening cross section	$A = a_{valve}/\pi r_0^2$		
Valve closure time	$T_c = \tau_c/\tau$		
Descriptive p	parameters		
Axial coordinate	$X = x/\lambda$		
Radial coordinate	$R = r/r_0$		
Axial flow velocity	$U_x = u_x/c$		
Time	$T = t/\tau$		

The simulations start with a stagnant fluid and continue for at least 5 contraction periods to eliminate the influence of the initial transient. This ensures that the difference in the results between consecutive periods does not exceed 1%.

We have previously extensively validated our FSI model with application to different flows including lymphatic pumping (Ballard et al., 2018; Hanasoge et al., 2017; Mao & Alexeev, 2014; Masoud et al., 2012; Yeh & Alexeev, 2016). Here, we perform two additional tests to examine the accuracy of the model for simulating flow generated due to moving vessel walls. The first test (Figure 3) compares the axial velocity profiles in vessels with radially moving walls with the analytical solutions for semi-infinite circular pipe flow with the same wall motion (Uchida & Aoki, 1977). The normalized radial velocity is defined as $\alpha = \frac{\rho v_r(t)r(t)}{\mu}$, where $v_r(t)$ is the radial speed and r(t) is the radial position. Three different normalized radial speeds were tested for expanding and contracting vessels. Normalized axial velocity profiles in Figure 3 indicate that the numerically calculated flow velocities are in close agreement with the analytical results for both expanding and contracting vessels.

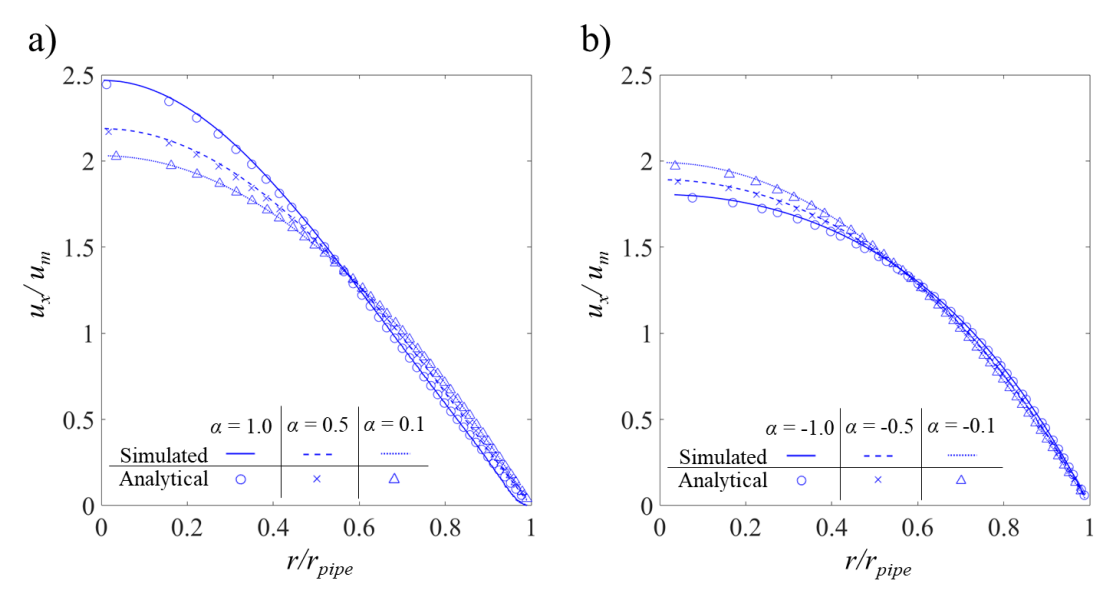


Figure 3. Axial flow velocity u_x in a) expanding and b) contracting vessels for different values of radial wall velocity α . Axial velocity is normalized by the mean axial velocity of the vessel u_m , whereas the radial coordinate r is normalized by the vessel radius r_{pipe} . The lines represent the simulated results, whereas the symbols represent the analytical solution (Uchida & Aoki, 1977).

The second test compared Q and W obtained using an analytical solution for peristaltic oscillation (Shapiro et al., 1969; Takabatake et al., 1988) with simulated results, as shown in Figure 4. The comparison is made for $\phi = 0.2$ and 0.25, $\Delta P = 0$ and 140, and for a range of Re. It was found that the simulations are close to the analytical solution under different system parameters relevant to our study. Divergence from the analytical solution growths as Re increases. This can be expected since the analytical solution assumes $Re \ll 1$.

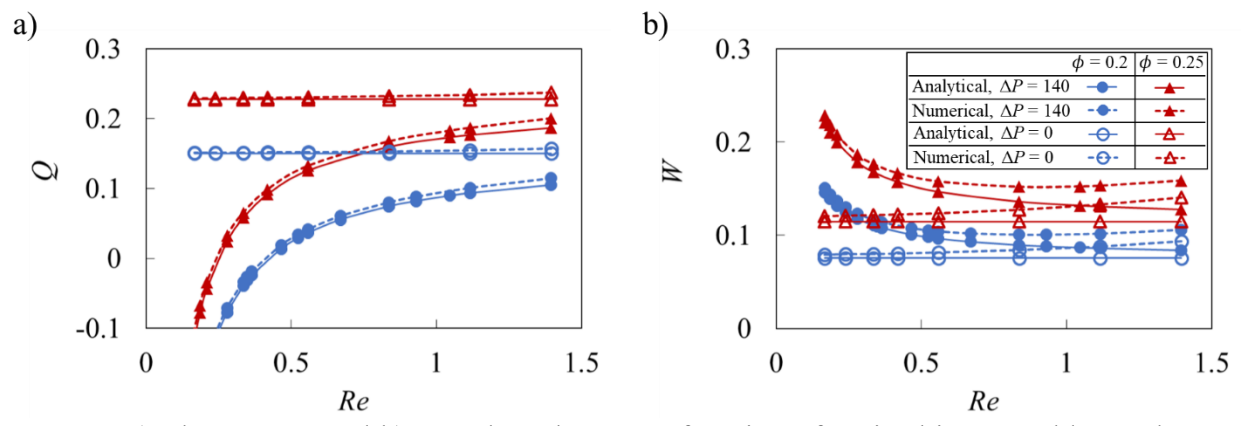


Figure 4. a) Flow rate Q and b) vessel work W as a function of peristaltic Reynolds number Re for different contraction amplitude ϕ without valves. The solid and dotted lines show the analytical and numerical solutions, respectively. The empty and filled symbols represent data for $\Delta P = 0$ and $\Delta P = 140$, respectively.

3. Results and discussion

3.1 Flow pattern

Figures 5a and 5b present snapshots showing axial velocity magnitude and valve deformation for different stages of the vessel contraction cycle, respectively, without and with adverse pressure gradient (see Video S3 in SI). Note that figures show one valve since the flow profile and valve deformation repeat due to their synchronous motion. Similar to peristaltic pumping without valves (Figure 1), the flow is divided into alternating packets of positive and negative axial velocities. Regions of the positive axial velocity travel in the expanded region of the vessel, while packets of negative axial velocity propagate within the contracted region of the vessel. This indicates that velocity packets propagate with the same speed as the contraction wave (Shapiro et al., 1969; Takabatake et al., 1988).

Unlike vessels without valves, velocity packets are disrupted when they pass through the elastic valves. Compared to an axisymmetric flow profile in the cases without valves, flow

disruption by the valves results in a flow that is no longer axisymmetric even though the pattern of alternating positive and negative velocity packets still persists. The valves open when they encounter packets of positive axial velocity and close to occlude the flow when packets of negative axial velocity pass. Thus, the valves affect the forward and backward flow in different ways. While the forward flow is allowed with some viscous loss due to the reduced orifice size, the backflow can be significantly suppressed and ultimately stopped by fully closed valves.

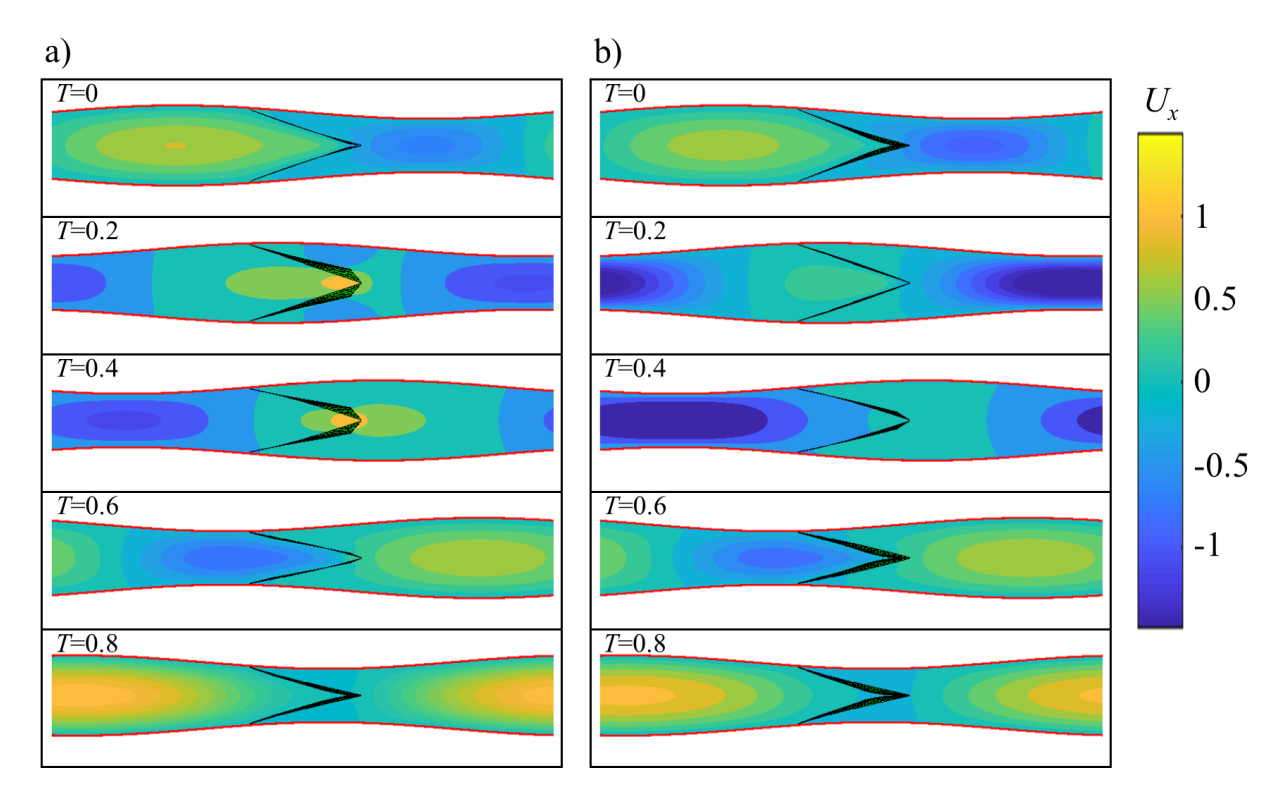


Figure 5. a) Axial flow velocity U_x at different instances of the contraction cycle in a valved vessel with no adverse pressure gradient. b) Axial flow velocity U_x in a valved vessel with $\Delta P = 140$. The flow profiles are shown at the symmetry plane perpendicular to the valve opening. Note that due to the valves, flow profile is not axisymmetric. The simulation parameters are $\phi = 0.2$, Re = 0.2, $K_b = 88$, and $K_s = 115$. See Video S3 in SI.

The valves deform differently when encountering fluid packets with positive and negative velocities, as shown in Figure 2d and in Video S2. When encountering packets of positive axial velocity, the leaflets stretch and deform outwards by a combined action of the flow and the vessel expansion. This process increases the opening area of the valve defined by the leaflet free edges, thereby enabling fluid flow. When the valve encounters negative velocity packets, the vessel contracts. The middle of the leaflets deforms inwards, allowing the free edges to rapidly collapse

and block the flow. The valve closure process culminates by creating a coaptation zone expanding from the leaflet free edges.

The effect of valves on backflow reduction is more evident when the flow is subjected to an adverse pressure gradient. In this scenario, a peristaltic vessel without a valve has a limited capacity to transport fluid in the direction of wave propagation (Figure 1b), whereas addition of unidirectional valves yields a positive net flow in the vessel (Figure 5b). Note that without adverse pressure gradient, both vessels with and without valves can successfully pump fluid in the positive direction (Figure 1a and Figure 5a). This further points to the important role that valves play in enabling pumping against adverse pressure gradients.

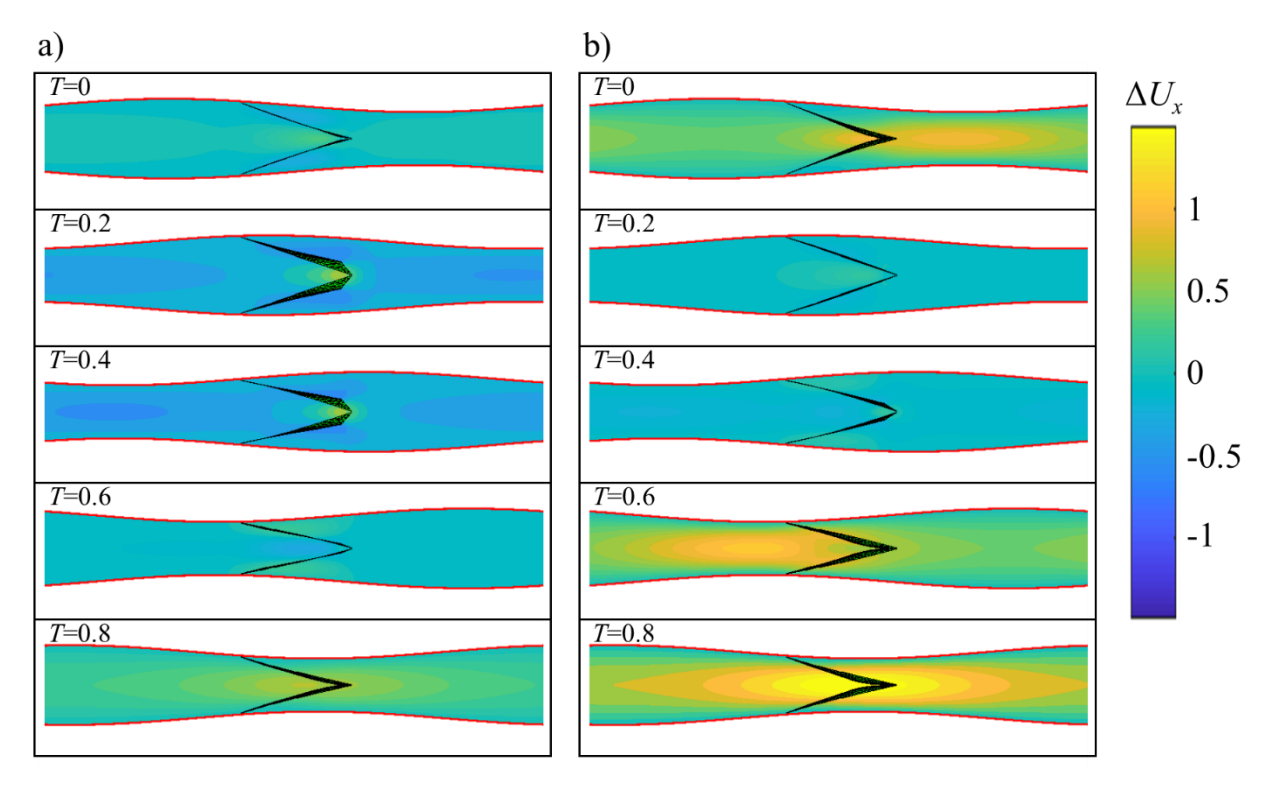


Figure 6. a) Axial flow velocity difference ΔU_x at different instances of the contraction cycle in a valved vessel with no adverse pressure gradient. b) Axial flow velocity difference ΔU_x in a valved vessel with $\Delta P = 140$. The flow profiles are shown at the symmetry plane perpendicular to the valve opening. The simulation parameters are $\phi = 0.2$, Re = 0.2, $K_b = 88$, and $K_s = 115$. The flow velocity difference ΔU_x is calculated as the difference between flow velocities in vessels with and without valves. See Video S4 in SI.

The effect of valves on pumping is further revealed when considering the difference in axial velocity between vessels with and without valves denoted as ΔU_x and shown in Figure 6 (see Video S4 in SI). When packets of positive velocity pass through an open valve (see Figure 6 for

T=0.2 and 0.4), the overall flow velocity pattern is similar to the flow in the valve-less vessel with minor flow disturbances around the valves, where the flow accelerates due to the reduced opening between the leaflets. In this case, ΔU_x is nearly zero everywhere in the vessel except for a small region in the vicinity of the valve. The velocity difference ΔU_x is more significant when vessel contraction passes the valve. In this case, negative flow velocity causes the valve to close and block the flow. This, in turn, results in a positive ΔU_x in most of the vessel, as shown in Figure 6 for T=0, 0.6, and 0.8. A significant positive difference in velocity between the cases with and without valves when the valves are closed indicates that the valves increase pumping by reducing backflow. Furthermore, when comparing Figures 6a and 6b, we find that the backflow reduction is more prominent when the pumping is against an adverse pressure gradient. Indeed, the adverse pressure gradient causes a significant negative flow when the valve-less vessel contracts (Figure 1b). The backflow is stopped by the closed valves in the case of the vessel fitted with valves (Figure 5b).

3.2 Effect of contraction wave speed on pumping

We examine the effect of contraction wave speed on pumping by varying the peristaltic Reynolds number that, in turn, is realized by varying the contraction period τ . In Figure 7, we show how the centerline flow velocity $U_x(0)$ changes along the vessel without an adverse pressure gradient at Re = 0.2 and Re = 0.6. The velocity is shown as a function of the distance along the vessel X and in the moving reference frame X - T. In Figures 7a and 7c, which show the velocity $U_x(0)$ as a function of the distance along the vessel X, the two vertical dotted lines indicate the location of the valve with the leaflet free edge being on the right side. Furthermore, the horizontal lines in these figures show the maximum and minimum magnitude of the centerline velocity in a vessel without a valve. Figures 7b and 7d show the velocity $U_x(0)$ in the moving reference frame X - T in which case the velocity in a valve-less vessel is represented by a single line. Note that the velocities in Figures 7a and 7b correspond to the snapshots shown in Figure 5a.

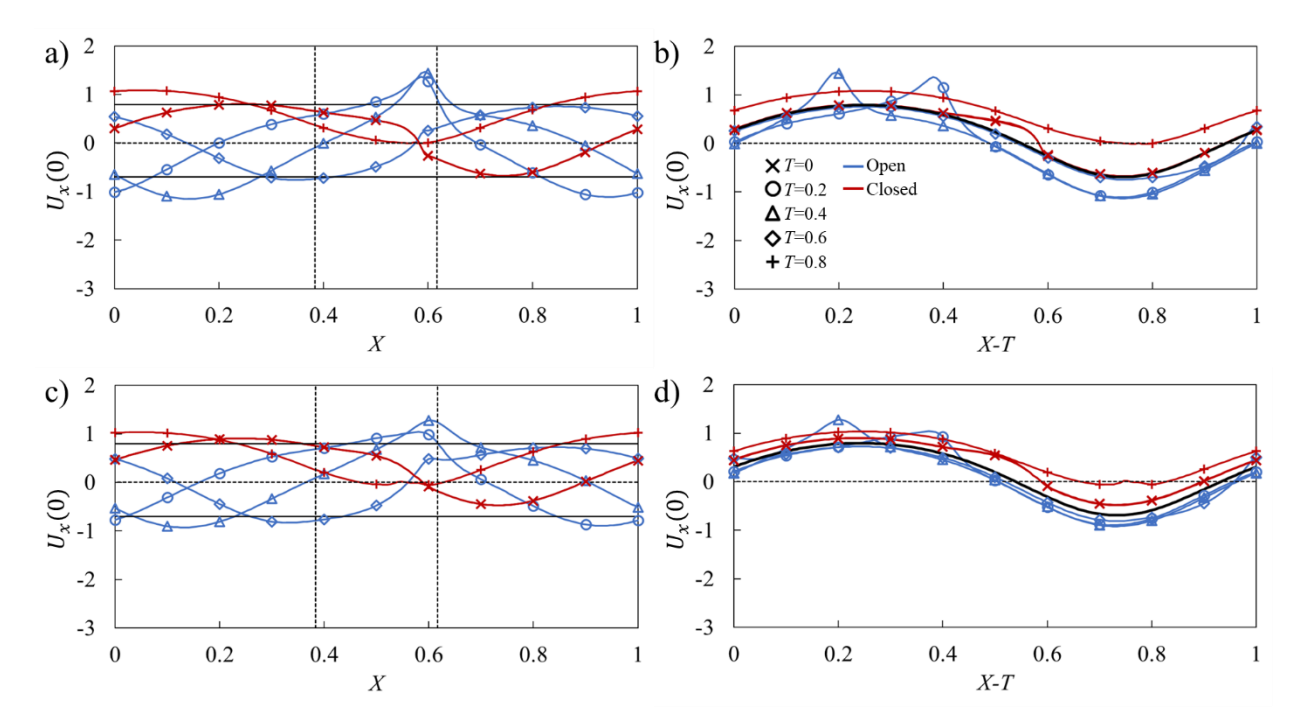


Figure 7. a) Centerline axial flow velocity $U_x(0)$ in the stationary reference frame in a vessel with no adverse pressure gradient with Re = 0.2. The maximum valve opening is $A_{max} = 0.44$. b) Same as a) but in the moving reference frame, the solid black line indicates the average centerline velocity for the valve-less vessel. c) Centerline axial flow velocity $U_x(0)$ in a stationary reference frame in a vessel with Re = 0.6. The maximum opening is $A_{max} = 0.68$. d) Same as c) but in the moving reference frame, the solid black line indicates the average centerline velocity for the valve-less vessel. The horizontal solid lines indicate the maximum and minimum centerline velocities in a vessel without valves. The dashed vertical lines indicate the boundaries of valve position. The blue and red lines show the velocities when the valves are, respectively, open $(A \ge 0.05)$ and closed (A < 0.05). The simulation parameters are $\Delta P = 0$, $\phi = 0.2$, $K_b = 88$, and $K_s = 115$.

Outside from the regions around the valve, the centerline velocity follows a sinusoidal wave (Figure 7a), which is characteristic for the centerline velocity in peristaltic vessels without valves (Figure 1c). The valves introduce a velocity disturbance that is manifested by a velocity maximum at the valve orifice located at X = 0.6 and is formed by the partially open leaflets at T = 0.2 and 0.4 (Figure 7a). Furthermore, when the valve is closed at T = 0, 0.6, and 0.8, the centerline velocity between coapted leaflets is nearly zero. Thus, the valve prevents a negative flow at the valve orifice.

To identify the velocity changes induced by the valves with respect to the centerline velocity in the valve-less vessel, we use a moving reference frame that is translated with the speed of the traveling wave (Figure 7b). We find that the valve can both decrease and increase the centerline velocity with respect to the valve-less vessel. The velocity corresponding to the open valve

condition is somewhat lower than the valve-less velocity. Thus, the flow resistance in the valves on average reduces the flow in the entire vessel. On the other hand, when the valve is closed, the centerline velocity in the vessel exceeds the valve-less velocity. For a fully closed valve, the velocity within the vessel is defined by the fluid redistribution induced by the peristaltic wave propagating along the vessel.

The overall pumping in the vessel with valves is greater than in a valve-less vessel when the backflow reduction due to valve closure outweighs the velocity decrease due to the hydrodynamic resistance in the open valve. Thus, the pumping performance is determined by the valve properties and is maximized when the valve is able to fully block the backflow with minimal resistance for the forward flow.

Increasing the Reynolds number from Re = 0.2 to Re = 0.6 does not change the general shape of the centerline velocity profile, although the maxima at the valve orifice are less pronounced (Figure 7c). During the backflow phase the valve is able to fully close as indicated by the near zero velocity at T = 0 and 0.8 at the leaflet edge. Compared to the case of Re = 0.2, the increase in wave speed decreases the deviation of centerline velocity from that of a valve-less vessel. We also find that the velocity during the open valve phase matches closer to the valve-less velocity with increased Reynolds number, which can be attributed to a reduced hydrodynamic resistance of the valve from a greater opening due to the faster fluid flow. Indeed, at Re = 0.2 the maximum opening of the valve is about 44% of the cross-sectional area under the average vessel diameter, whereas the maximum opening increases to 68% when Re = 0.6.

Figure 8 shows centerline velocities for the flow in vessels with Re = 0.2 and Re = 0.6 that experience an adverse pressure difference $\Delta P = 140$. The velocities in Figures 8a and 8b correspond to the snapshots in Figure 5b. An adverse pressure gradient has a minor effect on the shape of the velocity profiles compared to the case of the flow with $\Delta P = 0$ (Figure 7) although the velocities are shifted towards the negative values. For Re = 0.2, the valve-less vessel is unable to produce a net positive flow resulting in Q = -0.22. For the same Re, the vessel with the valves yields a small positive Q = 0.01, indicating that a sufficiently high ΔP can stop pumping by such vessels. Note that further increase of ΔP leads to the valve remaining fully closed throughout the entire contraction cycle. When compared to the velocity in the valve-less vessel, the velocities at the open valve condition are nearly identical to the valve-less velocity (Figure 8b). This can be attributed to a reduced flow through the valve at this ΔP as shown in Figure 8a.

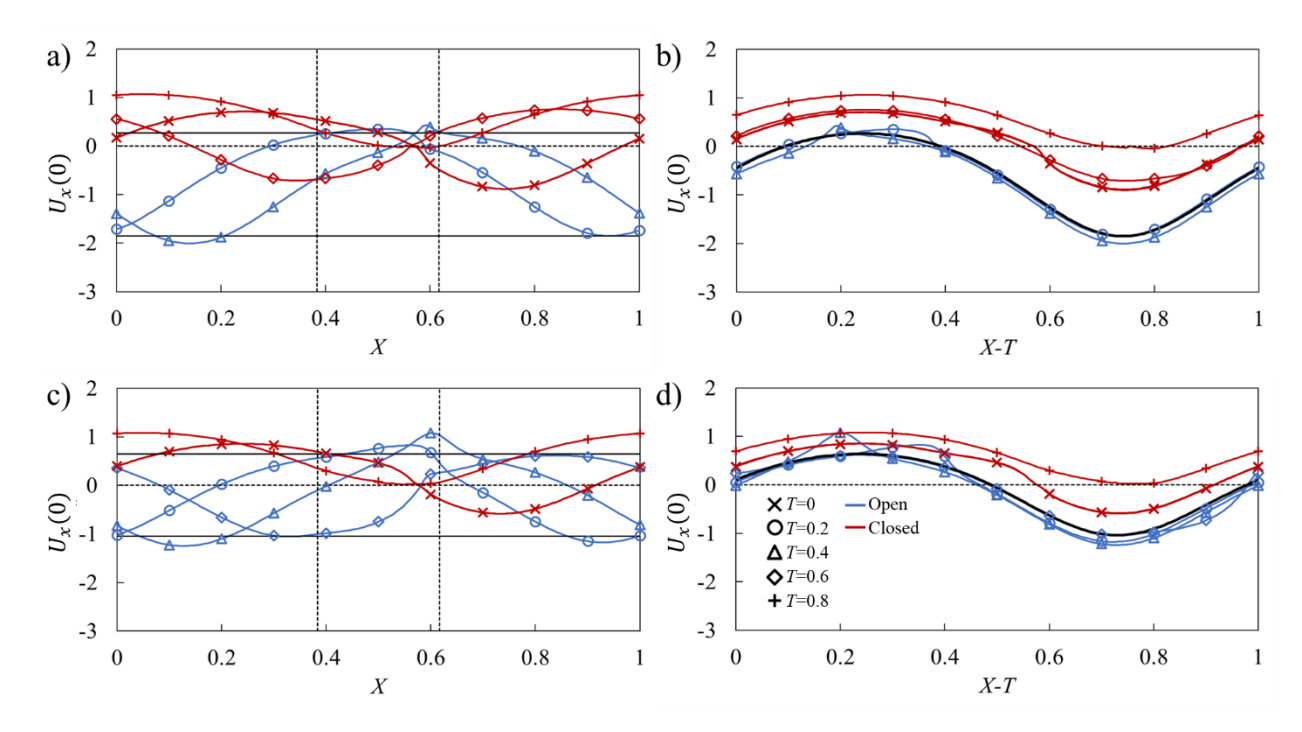


Figure 8. a) Centerline axial flow velocity $U_x(0)$ in the stationary reference frame in a vessel with Re = 0.2 with an adverse pressure gradient. The maximum valve opening is $A_{max} = 0.3$. b) Same as a) but in the moving reference frame, the solid black line indicates the average centerline velocity for the valve-less vessel. c) Centerline axial flow velocity $U_x(0)$ in a stationary reference frame in a vessel with Re = 0.6. The maximum opening is $A_{max} = 0.61$. d) Same as c) but in the moving reference frame, the solid black line indicates the average centerline velocity for the valve-less vessel. The horizontal solid lines indicate the maximum and minimum centerline velocities in vessels without valves. The dashed vertical lines indicate the boundaries of valve position. The blue and red lines show the velocities when the valves are, respectively, open $(A \ge 0.05)$ and closed (A < 0.05). The simulation parameters are $\Delta P = 140$, $\phi = 0.2$, $K_b = 88$, and $K_s = 115$.

At a larger Re = 0.6 (Figure 8c) both vessels with and without valves are able to generate a net positive fluid flow in spite of an adverse pressure gradient. However, valves enable significantly greater pumping of Q = 0.11 compared to Q = 0.04 without valves. This is again due to the ability of valves to stop backflow. The velocity during the open valve phase is slightly lower than the valve-less velocity (Figure 8d) and comparable to the velocity in the flow without adverse pressure gradient (Figure 7d). Indeed, in both cases normalized maximum valve openings are comparable with 61% and 68%, for $\Delta P = 140$ and $\Delta P = 0$, respectively. Thus, this adverse pressure gradient has a rather insignificant effect on the maximum valve opening.

Note that increasing *Re* has opposing effects on the peristaltic pumping with valves. On one hand, increasing *Re* facilitates valve opening and decreases the associated viscous loss; on the other hand, the time during which the valve is closed decreases impairing the valve's ability to

fully arrest the backflow. Indeed, at Re = 0.2 the valve is closed about 62% of the contraction cycle, whereas at Re = 0.6 the valve is closed about 42% of the contraction cycle.

The dependencies of the pumping parameters on Re are summarized in Figure 9. The data is shown for $\Delta P = 0$ using the empty symbols, and for $\Delta P = 140$ using the filled symbols. Figure 9a shows that normalized flow rate Q mostly increases as Re increases. Without an adverse pressure gradient, Q remains nearly flat in valve-less vessels and slightly increases when vessels are fitted with valves. Thus, the flow rate has nearly a linear relationship with the wave speed. When the pumping occurs against an adverse pressure gradient, Q rapidly decreases with decreasing Re. Without valves, low Re results in a negative Q, meaning that peristaltic pumping cannot overcome the adverse pressure gradient at these wave speeds. With valves, however, low Re leads to slightly positive values of Q, indicating that whereas peristatic motion cannot pump the fluid, the valves are able to eliminate the backflow.

Figure 9b shows the normalized work W done over a wave period by the peristaltic vessel. In valve-less cases and in valved cases with $\Delta P = 0$, W is nearly constant indicating that work done by the vessel increases nearly quadratically with Re since the normalization factor is proportional to Re^2 . Otherwise, the work W decreases with increasing Re, as increased flow rate leads to a larger valve opening and decreased loss from valve interference with the flow.

Pumping efficiency $\eta = q\Delta p_{\lambda}/w_{avg}$ is shown in Figure 9c as a function of Re. The efficiency is defined as the ratio between the work due to the fluid transport against the adverse pressure gradient and the work done by the vessel. Note that when $\Delta P = 0$ the efficiency is zero. We therefore present data only for $\Delta P = 140$. We find that the efficiency curves for vessels with and without valves exhibit maxima indicating the existence of optimum Re maximizing the pumping per unit work against an adverse pressure gradient. This result is consistent with the analytical solution for peristaltic pumping (Shapiro et al., 1969; Takabatake et al., 1988). The maxima of efficiency are a result of two opposing trends. At small Re, peristaltic pumping cannot overcome the adverse pressure gradient diminishing the flow rate and therefore the pumping efficiency. For higher Re, the flow rate increases as Re, whereas the work increases as Re^2 , leading to overall efficiency decrease with Re. Interestingly, valves increase the maximum efficiency and shift it to the lower values of Re. This can be related to a more rapid decrease of the flow rate with decreasing Re in valve-less vessels due to the adverse pressure gradient compared to vessels fitted with valves. Furthermore, the efficiency is greater for larger ϕ as a result of a faster flow (Figure 9a). For larger

Re, the efficiency of valve-less and valved vessels nearly overlaps, indicating a weak effect of valves on pumping in this flow regime.

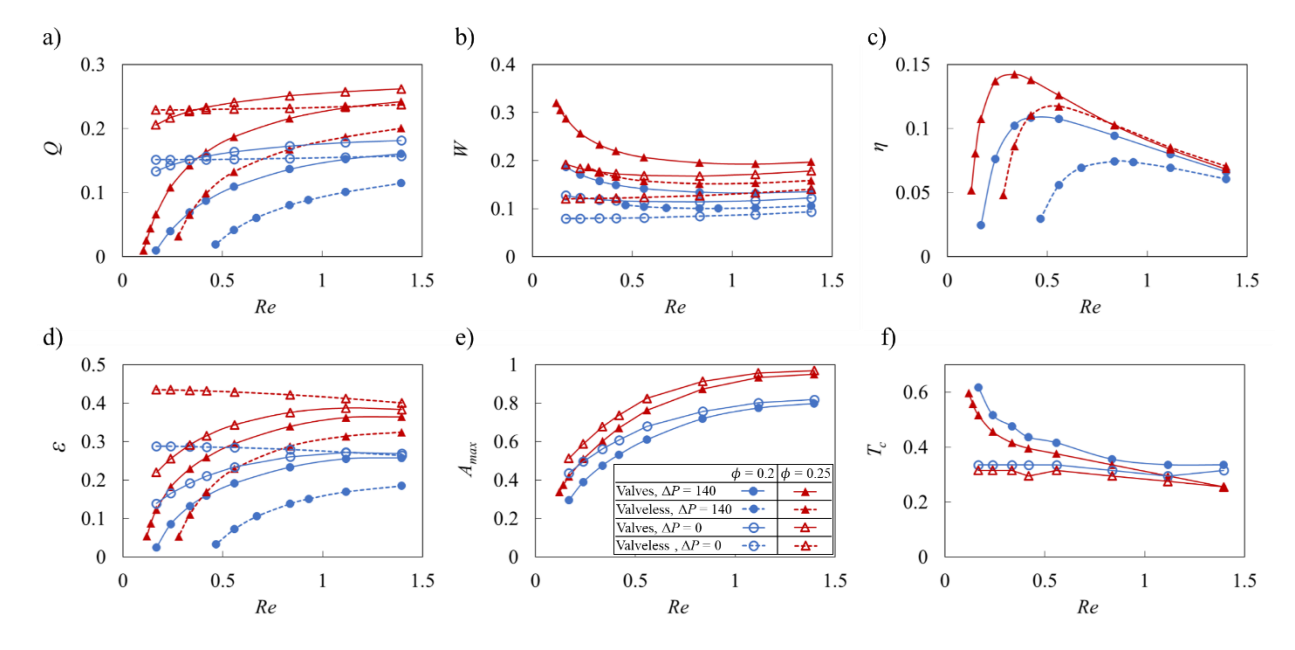


Figure 9. a) Flow rate, b) vessel work, c) pumping efficiency, d) pumping economy, e) maximum valve opening area A_{max} , and f) valve closure time T_c as a function of peristaltic Reynolds number for vessels with $K_b = 88$, and $K_s = 115$. The empty and filled symbols represent data $\Delta P = 0$ and $\Delta P = 140$, respectively. The dashed lines represent results from valve-less vessels. The valve is considered closed when A < 0.05.

Another metric to characterize the performance of the peristaltic pumping is flow economy ε shown in Figure 9d as a function of Re. In addition to accounting for the work against the adverse pressure gradient, as it is in the case for η , ε also accounts for the viscous losses in the vessel. We find that ε is significantly greater than η and closely resembles the trend of the normalized flow rate shown in Figure 9a, indicating that greater amount of work by the vessel goes to viscous loss than to pumping the fluid. Without an adverse pressure gradient, ε for the valve-less vessel exceeds the value for vessels with valves, due to the additional loss associated with valves restricting the flow. The difference decreases with increasing Re due to the larger valve opening (Figure 9e). However, when $\Delta P = 140$, ε for vessels with valves exceeds valve-less ε . Thus, adding valves improve the economy when the flow is confronted by an adverse pressure gradient, whereas without an adverse pressure, pumping of the valve-less vessel is more economical.

We further characterize valve behavior during peristaltic pumping by quantifying the maximum valve opening area A_{max} and the occlusion time T_c , which are shown as a function of

Re in respective Figures 9e and 9f. The maximum opening area steadily increases with Re and plateaus for Re > 1. For lower Re, an adverse pressure gradient somewhat decreases A_{max} as a result of a lower positive flow velocity in the vessel (Figure 8). The occlusion time T_c is relatively constant with Re when the flow is not affected by ΔP . This is consistent with the velocity profiles shown in Figure 7 that exhibit minor variations for different Re. On the other hand, an adverse pressure gradient causes T_c to increase with decreasing Re, as longer occlusion period occurs due to the increased backflow.

3.3 Effect of adverse pressure gradient on pumping

Figure 10 presents the dependence of peristaltic pumping parameters for vessels with and without valves on the magnitude of the adverse pressure difference ΔP . Here, we keep the wave speed constant leading to Re = 0.4. We find that the normalized flow rate Q decreases linearly with increasing ΔP (Figure 10a). Furthermore, Q increases with wave amplitude ϕ . For vessels without valves the decrease of Q is more rapid than for vessels with valves. As a result, valved vessels are able to pump fluid against significantly greater ΔP . However, this enhanced pumping in valved vessels comes at the cost of increased work W performed by the vessel (Figure 10b). The work by vessels with valves exceeds the work by valve-less vessels likely due to the increased viscous losses associated with the flow through the occluding valves. Increased wave amplitude ϕ results in greater W.

Pumping efficiency is presented in Figure 10c. In spite the greater work done by vessels with valves, their efficiency is either comparable (at lower ΔP) or exceeds (at higher ΔP) that of valveless vessels. Thus, in terms of pumping efficiency, the greater pumping capacity overcomes the increased viscous loss created by the valves. Furthermore, pumping efficiency curves exhibit maxima indicating the existence of optimum values of the adverse pressure gradient leading to the most efficient peristaltic pumping. For a vessel with valves, the optimum ΔP significantly exceeds that for a valve-less vessel. Furthermore, increasing ϕ increases the efficiency and the optimum ΔP . Thus, by changing vessel parameters the pumping can be optimized to a specific value of ΔP .

Flow economy shows nearly linear decrease with ΔP (Figure 10d). At lower ΔP , the work of vessel contraction mostly goes to overcome viscous friction loss rather than useful pumping. At these conditions, ε for valve-less vessels exceeds ε for vessels with valves. At higher ΔP , vessels

with valves exhibit better economy than valve-less vessels. Note that the economy is greater when the wave amplitude is increased.

The maximum valve opening area and valve occlusion time are shown in Figures 10e and 10f, respectively. Increasing adverse pressure gradient gradually decreases the valve maximum opening and increases the time that valve stays closed per contraction cycle. That is consistent with the reduction of the pumping flow rate with increasing ΔP (Figure 10a). Indeed, the slower flow velocity and lower favorable pressure gradient in the vessel decrease the forces acting to open the elastic valve resulting in lower A_{max} and longer T_c .

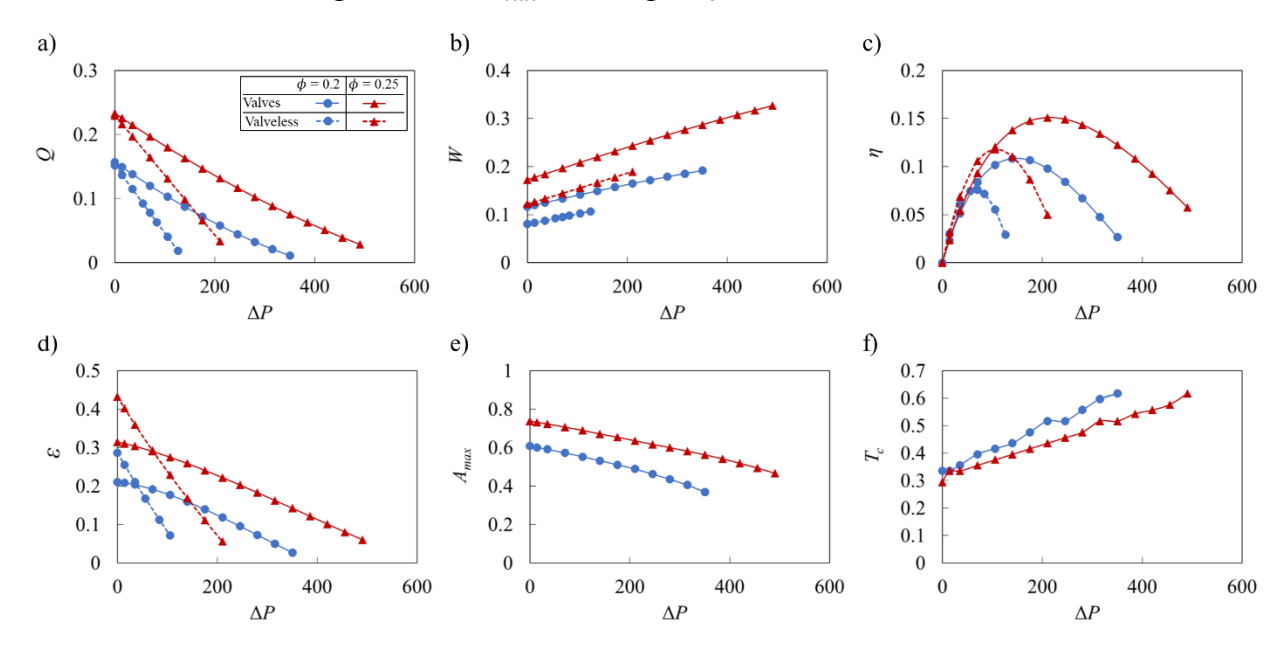


Figure 10. a) Flow rate, b) vessel work, c) pumping efficiency, d) pumping economy, e) maximum valve opening area A_{max} , and f) valve closure time T_c as a function of adverse pressure difference ΔP for vessels with Re = 0.4, $K_b = 88$, and $K_s = 115$. The dashed lines represent results from valve-less cases. The valve is considered closed when A < 0.05.

3.4 Effect of valve elastic properties on pumping

Figure 11 shows the side views of the valves with three representative bending stiffnesses, which we further refer as soft, normal, and stiff valves (see Video S5). The valves are plotted at different instances of vessel operation. Figure 11a indicates that soft valves experience valve depression at the middle of the valve under backflow. This deformation does not prevent backflow until the valve free ends fully close. Normal and stiff valves in Figures 11b and 11c experience closures at the valve free ends, leading to a more effective backflow prevention than the soft valve.

However, stiff valves are less responsive to changing flow rate, lengthening the time required for the valve to be fully open and closed, decreasing the maximum valve opening area during the forward flow and increasing the time the valve remains closed after the flow reversal.

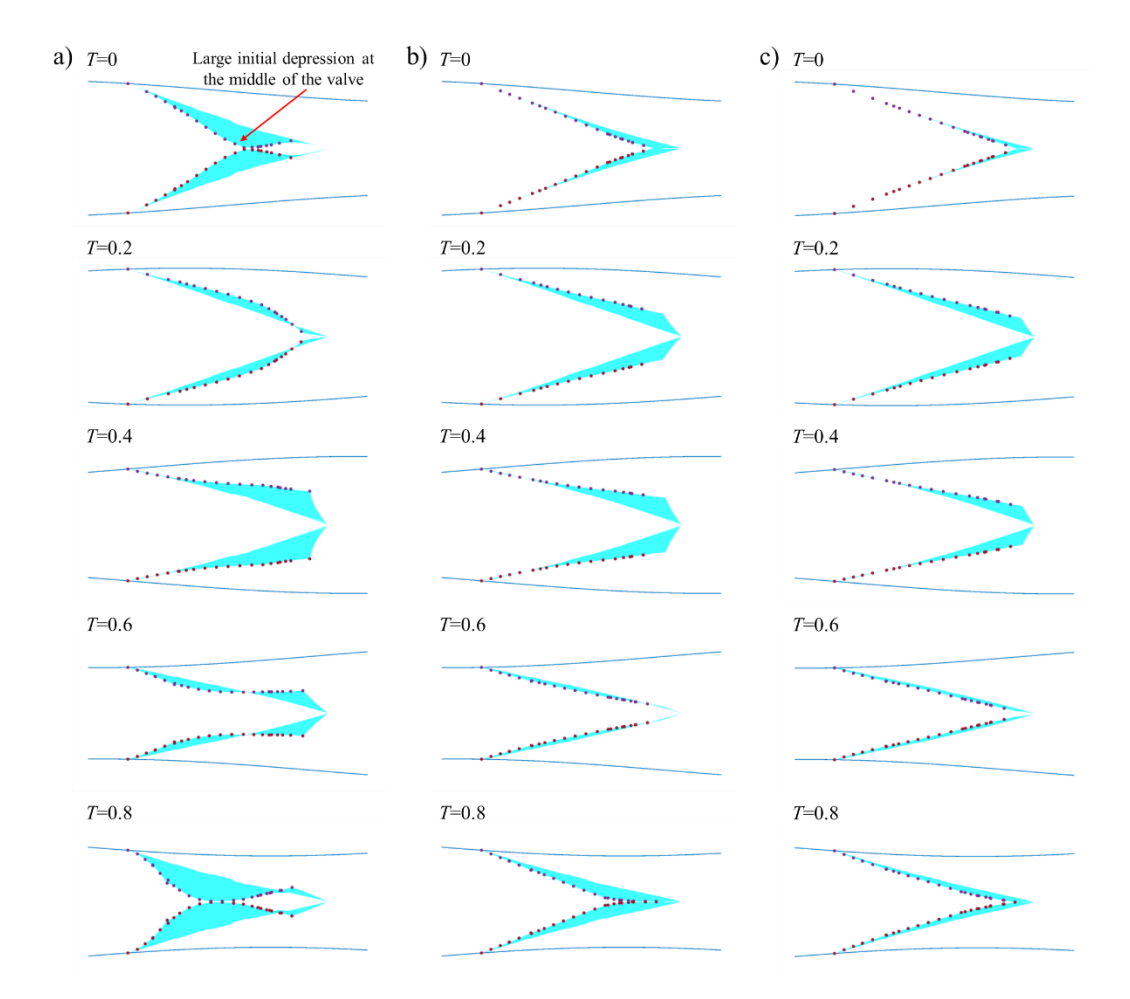


Figure 11. a) Deformation of valves with $K_b = 11$, b) with $K_b = 88$, c) with $K_b = 263$ at different instances of the vessel contraction cycle. The dots represent leaflet position at the centerline. The simulation parameters are $\Delta P = 140$, $\phi = 0.2$, Re = 0.4, and $K_s = 115$. See Video S5.

The behavior of the elastic valves can be further characterized by analyzing the time evolution of the flow rate Q_s and the leaflet cross-sectional opening area A that are shown in Figure 12 for flow with and without an adverse pressure gradient. The flow rate Q_s is averaged over the entire simulation domain. Note that for a valve-less vessel, Q_s remains constant as shown by the dotted lines in Figures 12a and 12c. Figures 12b and 12d also show the vessel radius at the valve location.

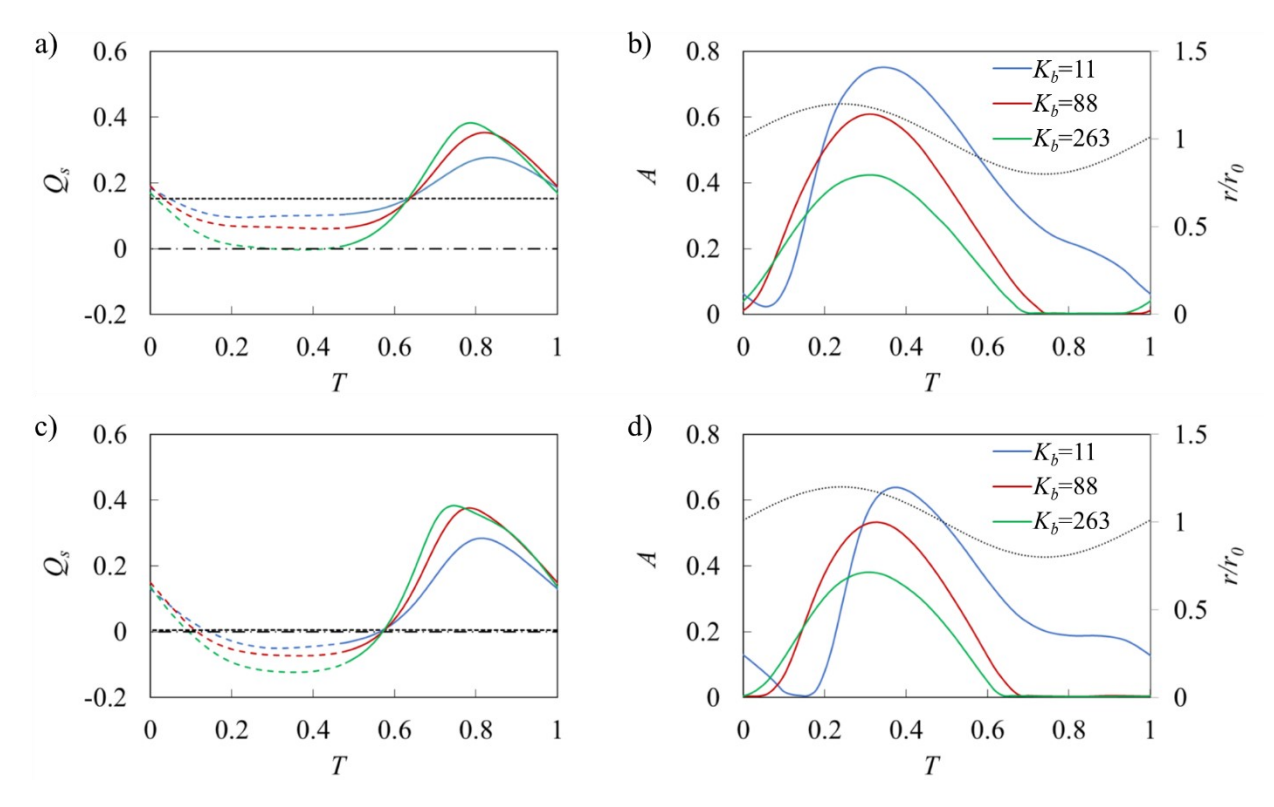


Figure 12. a) Time evolution of flow rate in vessels with $\Delta P = 0$. b) Time evolution of valve opening area A in vessels with $\Delta P = 0$. c) and d) are the same as a) and b) but with $\Delta P = 140$. The flow rate is averaged over contraction wavelength. The horizontal dashed line represents flow rate in the valve-less vessel while the dotted lines in b) and d) represent normalized vessel radius near the valve (r/r_0) . The dashed lines in a) and c) indicate that $r/r_0 > 1$, while the solid lines indicate that $r/r_0 < 1$. The horizontal dash-dot lines in a) and c) denote $Q_s = 0$. The simulation parameters are $\phi = 0.2$, Re = 0.4, and $K_s = 115$.

The valves open when the vessel diameter at the valve location increases (Figures 12b and 12d), which corresponds to the forward fluid flow through the valve (Figure 5). The valve opening is maximized when the vessel diameter is near its mean value. Softer valves can open more widely during flow through the valve and stay open longer. Furthermore, for such valves the opening starts later than for stiffer valves. Comparing the flow with and without an adverse pressure gradient we find that the adverse pressure gradient suppresses valve opening with the effect being more significant for softer valves. This can be attributed to the lower flow velocity and favorable pressure gradient for valve opening when the flow is affected by an adverse pressure.

The valve kinematics strongly affects the flow rate in the vessel (Figures 12b and 12d). When the valves are open, softer valves impose lower resistance on the flow leading to a faster flow. However, even with the softest valve, the instantaneous flow rate with an open valve is slower

than in the case of a valve-less vessel. When the valves are closed, the flow rate increases and exceeds the valve-less flow rate. Stiffer valves that close sooner enable a larger mean flow rate. Thus, during the oscillation period, the fluid is mostly pumped when the valves are closed, and the fluid is transported by the contracting wave propagating along the vessel. This behavior is more evident when the flow is confronted with an adverse pressure gradient (Figure 12c). In this case, the flow rate is negative when the valves are open, and the fluid is transported in the positive direction only when the valves are closed. Note that for the same adverse pressure gradient valve-less vessel generates a nearly zero net flow.

We therefore conclude that valve elasticity has opposing effects on the pumping performance. Softer valves enable greater valve opening, reducing viscous losses when the flow is moving in the positive directions through the valve. On the other hand, stiffer valves can close more rapidly during backflow minimizing flow reversal during this phase. This indicates that an optimum valve of elasticity exists that maximizes the vessel pumping performance.

Figure 13 presents the pumping parameters as a function of valve bending elasticity K_b for vessels with $\Delta P = 140$ and two wave amplitudes $\phi = 0.2$ and $\phi = 0.25$. We indeed find that the flow rate is maximized when $K_b \approx 63$ (Figure 13a). This optimum bending elasticity is about the same for both contraction wave amplitudes. The pumping efficiency and economy (Figures 13c and 13d) also exhibit maxima with K_b . Here, the optimum elasticity $K_b \approx 50$ is somewhat lower than that for the maximum flow rate.

We also find that work done by the vessel W gradually increases with increasing K_b (Figure 13b). The work increase is related to the higher viscous losses associated with less deformable valve leaflets (Ballard et al., 2018) that exhibit a lower valve opening area (Figure 13e). These figures show that this trend is independent of the wave amplitude. While A_{max} steadily decreases with increasing K_b , the time the valve stays closed T_c is nearly independent of K_b for $K_b > 50$, and sharply decreases for lower K_b . This indicates that softer valves are unable to properly close and fail to prevent the backflow in the vessel.

In Figure 13, we also examine the effect of the leaflet in-plane stiffness K_s on the valve performance. We compare valves with $K_s = 23$, 115, and 575. We find that a nearly 25-fold change of in-plane stiffness has a minor effect on the vessel parameters such as flow rate Q, work done by the vessel W, efficiency η , and economy ε . Only a slight decrease of A_{max} is found for the valves with $K_s = 575$ compared to the less stiff valves. Interestingly, the time that valve is

closed T_c is practically insensitive to changes in K_s . Thus, we conclude that the valve behavior is mostly defined by the valve bending elasticity whereas in-plane stiffness plays a minor role.

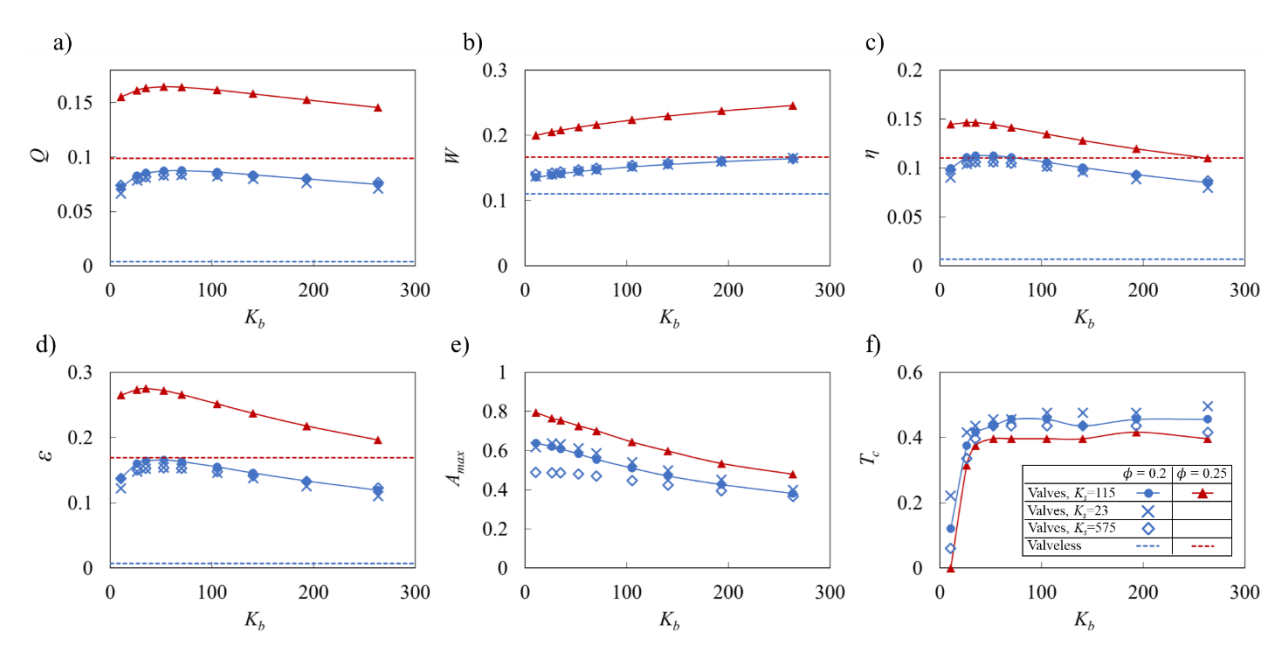


Figure 13. a) Flow rate, b) vessel work, c) pumping efficiency, d) pumping economy, e) the maximum valve opening area A_{max} , and f) valve closure time T_c as a function of valve bending stiffness K_b for vessels with $\Delta P = 140$ and Re = 0.4. The dashed lines represent results from valve-less cases. The valve is considered closed when A < 0.05.

The emergence of an optimum K_b indicates that the vessel mechanical properties can be optimized for specific pumping conditions. Furthermore, the optimum K_b leading to the fastest pumping performance and the highest efficiency and economy are somewhat different due to the dependency of W on K_b . Indeed, increasing W with K_b results in the softer valve being more efficient while providing slightly slower pumping. In Figure 14, we examine the dependency of the optimum valve elasticity on the magnitude of the adverse pressure gradient. The figure shows that the optimum elasticity increases with ΔP . We relate this trend to the improved ability of stiffer valves to withstand backflow due to an increasing adverse pressure gradient as such valves can close faster than softer valves (Figure 12d). When ΔP increases, flow rate in the vessel reduces and the ability to prevent the backflow has more significant effect on the pumping than increased viscous losses due to stiffer valves.

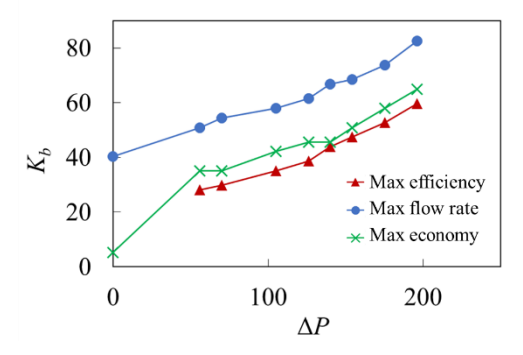


Figure 14. Optimal normalized bending stiffness yielding the maximum efficiency, economy, and flow rate under different adverse pressure gradients. The simulation parameters are $\phi = 0.2$, Re = 0.4, and $K_s = 115$.

3.5 Effect of contraction amplitude dependence on adverse pressure gradient

In the lymphatic system, the vessel contraction amplitude depends on the magnitude of the adverse pressure gradient (Davis et al., 2012). As shown in Figure 15, contraction amplitude gradually decreases with increasing ΔP . The decrease is more rapid for lower ΔP and the amplitude converges to a non-zero value when the pressure gradient increases beyond $\Delta P > 1000$ due to the inability of the lymphatic muscle cells to generate enough force for the pressure in the vessel proximal to the valve to exceed the pressure distal to the valve.

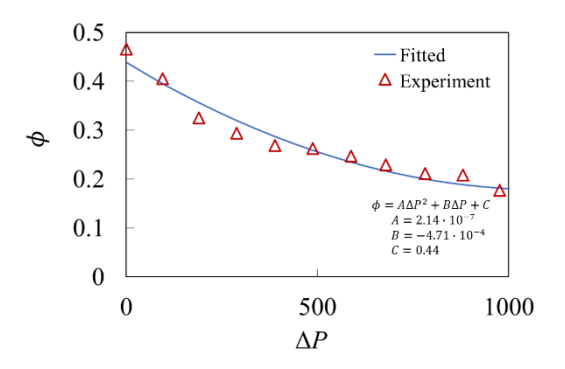


Figure 15. Contraction amplitude as a function of normalized pressure difference. Experimentally reported values (Davis et al., 2012) are shown by the triangles while the fit is shown by the solid line.

In Figure 16, we examine the effects of the pressure dependence of the contraction amplitude on the pumping performance. To isolate these effects, we compare normalized flow rate Q, work done by the vessel W, and pumping efficiency η for a vessel with pressure dependent contraction

amplitude to a vessel with a constant contraction amplitude. For the later vessel, we set the contraction amplitude such that the amplitudes for both vessels are identical when $\Delta P = 0$. The data is presented for two values of Re.

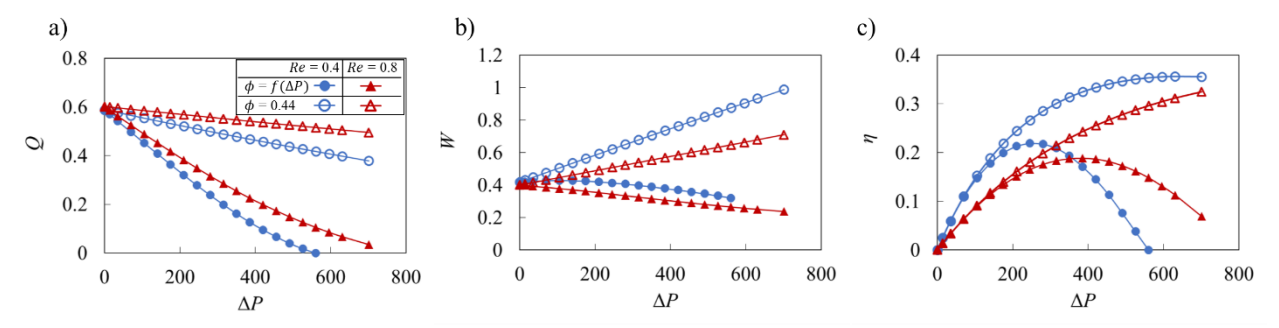


Figure 16. a) Flow rate, b) vessel work, and c) pumping efficiency as a function of the pressure gradient for vessels with and without pressure-dependent contraction amplitude. The valve elasticity is $K_b = 88$, and $K_s = 115$. Without adverse pressure gradient both the vessels exhibit an identical contraction amplitude of $\phi = 0.44$.

The simulations show that vessels with pressure dependent amplitude significantly underperform compared to the constant amplitude vessels, resulting in a rapid decrease of the pumping flow rate with increasing adverse pressure gradient (Figure 16a). This trend is consistent with the results shown in Figure 10a indicating a reduction in pumping rate with lower contraction amplitude. Pressure dependent contraction amplitude also has significant effect on the work done by the pumping vessel. As shown in Figure 16b, constant contraction amplitude leads to an increasing amount of work as the adverse pressure increases. By contrast, the pressure dependent amplitude results in work that is nearly independent from ΔP . This result suggests that lymphatic vessel contraction amplitude is limited by the work of contractile muscles driving vessel contraction and that once exposed to an adverse pressure gradient, lymphatic muscle quickly achieves maximum capacity in terms of the work generated. It is also interesting to note that the work only slightly changes with Re. Furthermore, pressure dependent contraction amplitude decreases the pumping efficiency compared to the constant amplitude case (Figure 16c). Although the work is roughly constant with pressure, the decreasing Q in the pressure dependent vessels results in a rapid decrease in efficiency when ΔP is sufficiently large. As a result, the optimum pumping occurs at lower values of ΔP compared to the vessels with a constant contraction amplitude.

4. Summary

Using fully coupled three-dimensional simulations, we investigate fluid pumping by a peristaltic vessel outfitted with elastic valves. The valves are formed by two adjusted angled elastic sheets representing a typical valve in a collecting lymphatic vessel. We compare fluid pumping by peristaltic vessels with and without valves to identify and isolate the effects of the valves on the resulting flow rate and pumping performance characterized in terms of pumping efficiency and economy. The simulations show that elastic valves increase the net fluid flow generated by a peristaltic vessel by reducing the backflow due to the periodic vessel contractions. At the same time, valves generate an additional flow resistance during the forward fluid flow. The effect of the valves on the pumping is more pronounced at lower Reynolds numbers and when the pumping is performed against an adverse pressure gradient. In both scenarios, the pumping by a valve-less peristaltic vessel diminishes due to a significant backflow.

We systematically investigate the effects of the vessel contraction wave speed, contraction amplitude, adverse pressure gradient, and valve elastic properties on the pumping performance. Increased vessel contraction wave speed and contraction amplitude increase pumping flow rate and work done by the vessel. Increasing adverse pressure gradient suppress fluid pumping while requiring greater work by the vessel. The valve stiffness exhibits an optimum maximizing the pumping flow rate. Higher valve stiffness increases viscous loss leading to an increased work, whereas softer valves close slowly enhancing backflow. The pumping economy is dominated by the viscous losses in the vessel and, thus, increases with increasing pumping flow rate. Optimal valve and vessel parameters exist that maximize the pumping efficiencies of valved peristaltic vessels. We find that the stiffer valves are required with increased adverse pressure gradients to maintain the high pumping efficiency. When the vessel amplitude decreases with increasing adverse pressure gradient in the manner it takes place in lymphatic systems, we find that vessel maintains a relatively constant work for the entire range of the pressure gradients, while gradually decreases the pumping flow rate. This result indicates that lymphatic vessel pumping is limited by the contractile capacity of lymphatic muscle.

Understanding valve mechanics in the lymphatic vasculature has become increasingly important. Oscillatory wall shear stress has been shown to enhance the expression of transcription factors necessary for the formation of lymphatic valves during development as well as for post-

natal valve maintenance (Cha et al., 2016; Cha et al., 2018; Choi et al., 2019; Sabine et al., 2012; Sabine et al., 2015). In addition mutations in mouse models in genes associated with primary lymphedema have produced valves that are dysfunctional at preventing backflow (Castorena-Gonzalez et al., 2020; Kazenwadel et al., 2015; Lapinski et al., 2012; Lapinski et al., 2017) and abnormal conduction of contraction waves (Castorena-Gonzalez et al., 2018). Thus, understanding the structure-function relationships that underpin proper valve performance and how subtle alterations in lymphatic structure and mechanics negatively impact over lymphatic transport is of high clinical importance. Moreover, knowledge of these structure-function relationships could also provide insight into the underlying mechanobiology that is driving the observed regional variation in lymphatic vessel pumping behavior and morphology (Gashev et al., 2004; Gashev et al., 2012; Zawieja et al., 2018). For example, it is possible that the regional differences in valve length and morphology in vessels close to the heart (such as the thoracic duct) compared to vessels found in the extremities could exist to optimize function in the context of the local mechanical loads placed on these vessels. Finally, our findings from this study can lead the development of simplified functional relationships between various valve properties and flow performance metrics, which can be incorporated into the existing lower dimensional models. Such simplified models are computationally less expensive enabling simulations of extensive lymphangion chains and their branched networks.

5. Acknowledgements

Financial support from the National Science Foundation (CMMI-1635133) and National Institutes of Health (1R01HL152152-01) are gratefully acknowledged.

References

- Akl, T. J., Coté, G. L., Nepiyushchikh, Z. V., Gashev, A. A. & Zawieja, D. C. 2011 Measuring contraction propagation and localizing pacemaker cells using high speed video microscopy. *Journal of biomedical optics*, **16**, 026016.
- Alexeev, A. & Balazs, A. C. 2007 Designing smart systems to selectively entrap and burst microcapsules. *Soft Matter*, **3**, 1500.
- Alexeev, A., Verberg, R. & Balazs, A. C. 2005 Modeling the motion of microcapsules on compliant polymeric surfaces. *Macromolecules*, **38**, 10244.
- Alexeev, A., Verberg, R. & Balazs, A. C. 2006 Designing compliant substrates to regulate the motion of vesicles. *Physical review letters*, **96**, 148103.
- Baish, J. W., Kunert, C., Padera, T. P. & Munn, L. L. 2016 Synchronization and Random Triggering of Lymphatic Vessel Contractions. *Plos Comput Biol*, **12**, e1005231.
- Ballard, M., Wolf, K. T., Nepiyushchikh, Z., Dixon, J. B. & Alexeev, A. 2018 Probing the effect of morphology on lymphatic valve dynamic function. *Biomechanics and modeling in mechanobiology*, **17**, 1343.
- Bertram, C. 2020 Modelling secondary lymphatic valves with a flexible vessel wall: how geometry and material properties combine to provide function. *Biomechanics and Modeling in Mechanobiology*.
- Bertram, C., Macaskill, C., Davis, M. & Moore, J. 2014a Development of a model of a multi-lymphangion lymphatic vessel incorporating realistic and measured parameter values. *Biomechanics and modeling in mechanobiology,* **13,** 401.
- Bertram, C., Macaskill, C. & Moore, J. 2011 Simulation of a chain of collapsible contracting lymphangions with progressive valve closure. *Journal of biomechanical engineering*, **133**, 011008.
- Bertram, C., Macaskill, C. & Moore, J. 2014b Incorporating measured valve properties into a numerical model of a lymphatic vessel. *Computer methods in biomechanics and biomedical engineering*, **17**, 1519.
- Bertram, C. D., Macaskill, C., Davis, M. J. & Moore, J. E. 2016 Consequences of intravascular lymphatic valve properties: a study of contraction timing in a multi-lymphangion model. *American Journal of Physiology-Heart and Circulatory Physiology*, **310**, H847.
- Böhme, G. & Müller, A. 2013 Analysis of non-Newtonian effects in peristaltic pumping. *Journal of Non-Newtonian Fluid Mechanics*, **201**, 107.
- Brouillard, P., Boon, L. & Vikkula, M. 2014 Genetics of lymphatic anomalies. *The Journal of clinical investigation*, **124**, 898.
- Burton-Opitz, R. & Nemser, R. 1917 The viscosity of lymph. *American Journal of Physiology-Legacy Content*, **45**, 25.
- Buxton, G. A., Verberg, R., Jasnow, D. & Balazs, A. C. 2005 Newtonian fluid meets an elastic solid: coupling lattice Boltzmann and lattice-spring models. *Physical Review E*, **71**, 056707.
- Castorena-Gonzalez, J. A., Zawieja, S. D., Li, M., Srinivasan, R. S., Simon, A. M., de Wit, C., de la Torre, R., Martinez-Lemus, L. A., Hennig, G. W. & Davis, M. J. 2018 Mechanisms of connexin-related lymphedema: a critical role for Cx45, but not Cx43 or Cx47, in the entrainment of spontaneous lymphatic contractions. *Circulation research*, 123, 964.
- Castorena-Gonzalez, J. A., Srinivasan, R. S., King, P. D., Simon, A. M. & Davis, M. J. 2020 Simplified method to quantify valve back-leak uncovers severe mesenteric lymphatic valve dysfunction in mice deficient in connexins 43 and 37. *The Journal of Physiology*.

- Cha, B., Geng, X., Mahamud, M. R., Fu, J., Mukherjee, A., Kim, Y., Jho, E.-h., Kim, T. H., Kahn, M. L. & Xia, L. 2016 Mechanotransduction activates canonical Wnt/β-catenin signaling to promote lymphatic vascular patterning and the development of lymphatic and lymphovenous valves. *Genes & development*, **30**, 1454.
- Cha, B., Geng, X., Mahamud, M. R., Zhang, J. Y., Chen, L., Kim, W., Jho, E.-h., Kim, Y., Choi, D. & Dixon, J. B. 2018 Complementary Wnt sources regulate lymphatic vascular development via PROX1-dependent Wnt/β-catenin signaling. *Cell reports*, **25**, 571.
- Choi, D., Park, E., Jung, E., Cha, B., Lee, S., Yu, J., Kim, P. M., Lee, S., Hong, Y. J. & Koh, C. J. 2019 Piezo1 incorporates mechanical force signals into the genetic program that governs lymphatic valve development and maintenance. *JCI insight*, 4.
- Connington, K., Kang, Q., Viswanathan, H., Abdel-Fattah, A. & Chen, S. 2009 Peristaltic particle transport using the lattice Boltzmann method. *Physics of Fluids*, **21**, 053301.
- Davis, M. J., Rahbar, E., Gashev, A. A., Zawieja, D. C. & Moore, J. E. 2011 Determinants of valve gating in collecting lymphatic vessels from rat mesentery. *Am. J. Physiol. Heart Circ. Physiol.*, **301**, H48.
- Davis, M. J., Scallan, J. P., Wolpers, J. H., Muthuchamy, M., Gashev, A. A. & Zawieja, D. C. 2012 Intrinsic increase in lymphangion muscle contractility in response to elevated afterload. *American Journal of Physiology-Heart and Circulatory Physiology*, **303**, H795.
- Dixon, J. B. 2010 Lymphatic lipid transport: sewer or subway? *Trends in Endocrinology & Metabolism*, **21**, 480.
- Eisenhoffer, J., Kagal, A., Klein, T. & Johnston, M. 1995 Importance of valves and lymphangion contractions in determining pressure gradients in isolated lymphatics exposed to elevations in outflow pressure. *Microvasc. Res.*, **49**, 97.
- Gashev, A. A., Davis, M. J., Delp, M. D. & Zawieja, D. C. 2004 Regional variations of contractile activity in isolated rat lymphatics. *Microcirculation*, **11**, 477.
- Gashev, A. A., Davis, M. J. & Zawieja, D. C. 2002 Inhibition of the active lymph pump by flow in rat mesenteric lymphatics and thoracic duct. *The Journal of physiology*, **540**, 1023.
- Gashev, A. A., Zhang, R.-Z., Muthuchamy, M., Zawieja, D. C. & Davis, M. J. 2012 Regional heterogeneity of length—tension relationships in rat lymph vessels. *Lymphatic research and biology*, **10**, 14.
- Hanasoge, S., Ballard, M., Hesketh, P. J. & Alexeev, A. 2017 Asymmetric motion of magnetically actuated artificial cilia. *Lab Chip*, **17**, 3138.
- Hariharan, P., Seshadri, V. & Banerjee, R. K. 2008 Peristaltic transport of non-Newtonian fluid in a diverging tube with different wave forms. *Mathematical and Computer Modelling*, **48**, 998.
- Ikomi, F. & Schmid-Schonbein, G. 1996 Lymph pump mechanics in the rabbit hind leg. *American Journal of Physiology-Heart and Circulatory Physiology*, **271**, H173.
- Jamalian, S., Bertram, C. D., Richardson, W. J. & Moore, J. E. 2013 Parameter sensitivity analysis of a lumped-parameter model of a chain of lymphangions in series. *Am. J. Physiol. Heart Circ. Physiol.*, **305**, H1709.
- Jamalian, S., Davis, M. J., Zawieja, D. C. & Moore, J. E. 2016 Network scale modeling of lymph transport and its effective pumping parameters. *PloS one*, **11**, e0148384.
- Kassis, T., Yarlagadda, S. C., Kohan, A. B., Tso, P., Breedveld, V. & Dixon, J. B. 2016 Postprandial lymphatic pump function after a high-fat meal: a characterization of contractility, flow, and viscosity. *American Journal of Physiology-Gastrointestinal and Liver Physiology*, **310**, G776.

- Kazenwadel, J., Betterman, K. L., Chong, C.-E., Stokes, P. H., Lee, Y. K., Secker, G. A., Agalarov, Y., Demir, C. S., Lawrence, D. M. & Sutton, D. L. 2015 GATA2 is required for lymphatic vessel valve development and maintenance. *The Journal of clinical investigation*, **125**, 2979.
- Kornuta, J. A., Nepiyushchikh, Z., Gasheva, O. Y., Mukherjee, A., Zawieja, D. C. & Dixon, J. B. 2015 Effects of dynamic shear and transmural pressure on wall shear stress sensitivity in collecting lymphatic vessels. *American Journal of Physiology-Regulatory, Integrative and Comparative Physiology*, **309**, R1122.
- Kunert, C., Baish, J. W., Liao, S., Padera, T. P. & Munn, L. L. 2015 Mechanobiological oscillators control lymph flow. *Proceedings of the National Academy of Sciences*, **112**, 10938.
- Ladd, A. & Verberg, R. 2001 Lattice-Boltzmann simulations of particle-fluid suspensions. *Journal of statistical physics*, **104**, 1191.
- Lapinski, P. E., Kwon, S., Lubeck, B. A., Wilkinson, J. E., Srinivasan, R. S., Sevick-Muraca, E. & King, P. D. 2012 RASA1 maintains the lymphatic vasculature in a quiescent functional state in mice. *The Journal of clinical investigation*, **122**, 733.
- Lapinski, P. E., Lubeck, B. A., Chen, D., Doosti, A., Zawieja, S. D., Davis, M. J. & King, P. D. 2017 RASA1 regulates the function of lymphatic vessel valves in mice. *The Journal of clinical investigation*, **127**, 2569.
- Lauweryns, J. M. & Boussauw, L. 1973 The ultrastructure of lymphatic valves in the adult rabbit lung. *Zeitschrift für Zellforschung und Mikroskopische Anatomie*, **143**, 149.
- MacDonald, A. J., Arkill, K. P., Tabor, G. R., McHale, N. G. & Winlove, C. P. 2008 Modeling flow in collecting lymphatic vessels: one-dimensional flow through a series of contractile elements. *Am. J. Physiol. Heart Circ. Physiol.*, **295**, H305.
- Mao, W. & Alexeev, A. 2014 Motion of spheroid particles in shear flow with inertia. *Journal of Fluid Mechanics*, **749**, 145.
- Margaris, K. & Black, R. A. 2012 Modelling the lymphatic system: challenges and opportunities. *J. R. Soc. Interface*, **9**, 601.
- Masoud, H., Bingham, B. I. & Alexeev, A. 2012 Designing maneuverable micro-swimmers actuated by responsive gel. *Soft Matter*, **8**, 8944.
- McGeown, J., McHale, N. & Thornbury, K. 1988 Arterial pulsation and lymph formation in an isolated sheep hindlimb preparation. *The Journal of physiology*, **405**, 595.
- Moore, J. E. & Bertram, C. D. 2018 Lymphatic system flows. *Annual review of fluid mechanics*, **50**, 459.
- Mortimer, P. S. & Rockson, S. G. 2014 New developments in clinical aspects of lymphatic disease. *The Journal of clinical investigation*, **124**, 915.
- Ohhashi, T., Azuma, T. & Sakaguchi, M. 1980 Active and passive mechanical characteristics of bovine mesenteric lymphatics. *American Journal of Physiology-Heart and Circulatory Physiology*, **239**, H88.
- Ostoja-Starzewski, M. 2002 Lattice models in micromechanics. Appl. Mech. Rev., 55, 35.
- Pan, W. R., le Roux, C. M. & Levy, S. M. 2011 Alternative lymphatic drainage routes from the lateral heel to the inguinal lymph nodes: anatomic study and clinical implications. *ANZ journal of surgery*, **81**, 431.
- Pan, W. R., Le Roux, C. M., Levy, S. M. & Briggs, C. A. 2010 The morphology of the human lymphatic vessels in the head and neck. *Clinical Anatomy*, **23**, 654.

- Petrova, T. V., Karpanen, T., Norrmén, C., Mellor, R., Tamakoshi, T., Finegold, D., Ferrell, R., Kerjaschki, D., Mortimer, P. & Ylä-Herttuala, S. 2004 Defective valves and abnormal mural cell recruitment underlie lymphatic vascular failure in lymphedema distichiasis. *Nature medicine*, **10**, 974.
- Pozrikidis, C. 1987 A study of peristaltic flow. Journal of Fluid Mechanics, 180, 515.
- Quick, C. M., Venugopal, A. M., Gashev, A. A., Zawieja, D. C. & Stewart, R. H. 2007 Intrinsic pump-conduit behavior of lymphangions. *American Journal of Physiology-Regulatory, Integrative and Comparative Physiology*, **292**, R1510.
- Rachid, H. & Ouazzani, M. 2015 Mechanical efficiency of peristaltic pumping of a Newtonian fluid between two deformable coaxial tubes with different phases and amplitudes. *The European Physical Journal Plus*, **130**, 122.
- Rahbar, E. & Moore, J. E. 2011 A model of a radially expanding and contracting lymphangion. *J. Biomech.*, **44**, 1001.
- Rao, A. R. & Usha, S. 1995 Peristaltic transport of two immiscible viscous fluids in a circular tube. *Journal of Fluid Mechanics*, **298**, 271.
- Razavi, M. S., Nelson, T. S., Nepiyushchikh, Z., Gleason, R. L. & Dixon, J. B. 2017 The relationship between lymphangion chain length and maximum pressure generation established through in vivo imaging and computational modeling. *Am. J. Physiol. Heart Circ. Physiol.*, **313**, H1249.
- Reddy, N. P., Krouskop, T. A. & Newell Jr, P. H. 1977 A computer model of the lymphatic system. *Computers in biology and medicine*, **7**, 181.
- Reddy, N. P., Palmieri, V. & Cochran, G. 1981 Subcutaneous interstitial fluid pressure during external loading. *American Journal of Physiology-Regulatory, Integrative and Comparative Physiology*, **240**, R327.
- Sabine, A., Agalarov, Y., Maby-El Hajjami, H., Jaquet, M., Hägerling, R., Pollmann, C., Bebber, D., Pfenniger, A., Miura, N. & Dormond, O. 2012 Mechanotransduction, PROX1, and FOXC2 cooperate to control connexin37 and calcineurin during lymphatic-valve formation. *Developmental cell*, **22**, 430.
- Sabine, A., Bovay, E., Demir, C. S., Kimura, W., Jaquet, M., Agalarov, Y., Zangger, N., Scallan, J. P., Graber, W. & Gulpinar, E. 2015 FOXC2 and fluid shear stress stabilize postnatal lymphatic vasculature. *The Journal of clinical investigation*, **125**, 3861.
- Scallan, J. P., Wolpers, J. H., Muthuchamy, M., Zawieja, D. C., Gashev, A. A. & Davis, M. J. 2012 Independent and interactive effects of preload and afterload on the pump function of the isolated lymphangion. *American Journal of Physiology-Heart and Circulatory Physiology*, **303**, H809.
- Shapiro, A. H., Jaffrin, M. Y. & Weinberg, S. L. 1969 Peristaltic pumping with long wavelengths at low Reynolds number. *Journal of fluid mechanics*, **37**, 799.
- Skalak, T., Schmid-Schönbein, G. & Zweifach, B. 1984 New morphological evidence for a mechanism of lymph formation in skeletal muscle. *Microvascular research*, **28**, 95.
- Succi, S. 2001 *The lattice Boltzmann equation: for fluid dynamics and beyond*: Oxford university press.
- Sutera, S. P. & Skalak, R. 1993 The history of Poiseuille's law. Annu. Rev. Fluid Mech., 25, 1.
- Swartz, M. A. 2001 The physiology of the lymphatic system. Adv. Drug Deliver. Rev., 50, 3.
- Takabatake, S., Ayukawa, K. & Mori, A. 1988 Peristaltic pumping in circular cylindrical tubes: a numerical study of fluid transport and its efficiency. *Journal of Fluid Mechanics*, **193**, 267.

- Tripathi, D. 2013 Study of transient peristaltic heat flow through a finite porous channel. *Mathematical and Computer Modelling*, **57**, 1270.
- Uchida, S. & Aoki, H. 1977 Unsteady flows in a semi-infinite contracting or expanding pipe. *Journal of Fluid Mechanics*, **82**, 371.
- Watson, D. J., Sazonov, I., Zawieja, D. C., Moore, J. E. & van Loon, R. 2017 Integrated geometric and mechanical analysis of an image-based lymphatic valve. *Journal of biomechanics*, **64**, 172.
- Webb Jr, R. C. & Starzl, T. 1953 The effect of blood vessel pulsations on lymph pressure in large lymphatics. *Bulletin of the Johns Hopkins Hospital*, **93**, 401.
- Wilson, J. T., van Loon, R., Wang, W., Zawieja, D. C. & Moore, J. E. 2015 Determining the combined effect of the lymphatic valve leaflets and sinus on resistance to forward flow. *J. Biomech.*, **48**, 3584.
- Yeh, P. D. & Alexeev, A. 2016 Effect of aspect ratio in free-swimming plunging flexible plates. *Computers & Fluids*, **124**, 220.
- Zawieja, D. C. 2009 Contractile physiology of lymphatics. *Lymphatic research and biology*, **7**, 87.
- Zawieja, D. C., Davis, K. L., Schuster, R., Hinds, W. M. & Granger, H. J. 1993 Distribution, propagation, and coordination of contractile activity in lymphatics. *American Journal of Physiology-Heart and Circulatory Physiology*, **264**, H1283.
- Zawieja, S. D., Castorena-Gonzalez, J. A., Scallan, J. P. & Davis, M. J. 2018 Differences in L-type Ca2+ channel activity partially underlie the regional dichotomy in pumping behavior by murine peripheral and visceral lymphatic vessels. *American Journal of Physiology-Heart and Circulatory Physiology*, **314**, H991.
- Zien, T.-F. & Ostrach, S. 1970 A long wave approximation to peristaltic motion. *Journal of Biomechanics*, **3**, 63.